REVIEW ARTICLE | MAY 28 2026

Coherent nonlinear vibrational microscopy

Kuan Luo ; Dongsheng Hu ; Jiaying Li ; Yue Yu ; Ke Xue ; Yuan Ji ; Fan Yang ; Jianpeng Ao ; Minbiao Ji

Appl. Phys. Rev. 13, 021329 (2026)
https://doi.org/10.1063/5.0313530

Applied Physics Reviews REVIEW pubs.aip.org/aip/are

Coherent nonlinear vibrational microscopy

Cite as: Appl. Phys. Rev. **13**, 021329 (2026); doi: 10.1063/5.0313530
Submitted: 23 November 2025 · Accepted: 11 May 2026 ·
Published Online: 28 May 2026

Kuan Luo,[1] Dongsheng Hu,[1] Jiaying Li,[1] Yue Yu,[1] Ke Xue,[2,a)] Yuan Ji,[3,a)] Fan Yang,[4,a)] Jianpeng Ao,[1,a)] and Minbiao Ji[1,a)]

AFFILIATIONS

[1]State Key Laboratory of Surface Physics and Department of Physics, Shanghai Key Laboratory of Metasurfaces for Light Manipulation, Endoscopy Center and Endoscopy Research Institute, Zhongshan Hospital, Fudan University, 200433 Shanghai, China
[2]Department of Plastic Surgery, Pudong Gongli Hospital, Shanghai University of Medicine & Health Sciences, 200135 Shanghai, China
[3]Department of Pathology, Zhongshan Hospital, Fudan University, 200032 Shanghai, China
[4]Shanghai Institute of Optics and Fine Mechanics, Chinese Academy of Sciences, Shanghai, China

[a)]**Authors to whom correspondence should be addressed:** nanxuebeiyuan@126.com; ji.yuan@zs-hospital.sh.cn; yang@siom.ac.cn; 20110190072@fudan.edu.cn; and minbiaoj@fudan.edu.cn

ABSTRACT

Coherent nonlinear vibrational microscopy has emerged as a powerful platform for label-free, chemically specific imaging by probing intrinsic chemical bond vibrations. This review comprehensively examines the principles and applications of three foundational techniques: vibrational sum-frequency generation for interfacial and chiral analysis; coherent Raman scattering, encompassing coherent anti-Stokes Raman scattering and stimulated Raman scattering, for bond-selective chemical visualization; and stimulated Brillouin scattering for biomechanical mapping. We highlight recent transformative advances including hyperspectral multiplexing, super-resolution implementations, and AI-integrated analysis, which have significantly enhanced imaging capabilities. These developments have enabled unique applications in diverse fields such as biomedicine, physical chemistry, materials science, and environmental science. While challenges in imaging depth and system portability remain, we discuss promising solutions based on ongoing instrumental and computational developments. Collectively, these coherent nonlinear vibrational imaging techniques bridge molecular spectroscopy and functional microscopy with unprecedented analytical and diagnostic capabilities.

TABLE OF CONTENTS

I. INTRODUCTION

Since the invention of the optical microscope, microscopic imaging technologies have continuously advanced our understanding of cellular and subcellular architecture as well as dynamic biological processes.[1] Subsequently, the emergence of contrast-enhanced modalities such as phase-contrast microscopy enabled visualization of intracellular organelles in living cells without the need for staining.[2] With the development of fluorescent probes, fluorescence microscopy has allowed molecular-level visualization of structures within biological specimens.[3,4] Integrated with advanced modalities such as multiphoton excitation,[5,6] light-sheet illumination,[7] and various super-resolution techniques,[8,9] fluorescence microscopy enables high-resolution visualization of subcellular architecture and real-time monitoring of biochemical dynamics within living cells. It has become an indispensable platform for elucidating spatial organization and molecular interactions underlying biological systems.[10] However, the molecular size and physicochemical properties of fluorophores often differ substantially from those of their native small-molecule or protein targets, potentially inducing biological perturbations during conjugation and photophysical processes. The broad emission bandwidth and susceptibility to photobleaching also constrain multiplexing capacity and long-term imaging performance.[11,12]

To circumvent the reliance on external labels, vibrational spectroscopic imaging has emerged as a powerful label-free approach that exploits intrinsic molecular bond vibrations to provide chemically specific contrast. Such as in spontaneous Raman scattering[13] and infrared (IR) absorption spectroscopy,[14] molecular vibrations serve as natural fingerprints for chemical identification. While spontaneous Raman scattering offers high molecular specificity, its inherently weak scattering cross section leads to low signal levels that necessitate long acquisition times.[15] Conversely, IR absorption achieves stronger signals but suffers from poor spatial resolution due to the long wavelength of mid-infrared light and severe water absorption, limiting *in vivo* imaging capability.[16,17] As a result, linear vibrational modalities face a trade-off between chemical sensitivity and spatial resolution, posing challenges for high-speed, high-resolution imaging in complex biological systems.

Nonlinear vibrational microscopy overcomes these constraints through higher-order optical interactions. By leveraging nonlinear susceptibilities, these approaches deliver orders-of-magnitude signal enhancement, improved signal-to-noise ratios (SNRs), and intrinsic three-dimensional optical sectioning. Representative modalities include vibrational sum-frequency generation (VSFG),[18] coherent Raman scattering (CRS),[19] and stimulated Brillouin scattering (SBS) microscopy.[20] Over the past decade, nonlinear vibrational microscopy has evolved into a versatile imaging platform enabling rapid hyperspectral acquisition, volumetric three-dimensional mapping, and super-resolution imaging.

In parallel, mid-infrared photothermal microscopy has made rapid progress as a powerful vibrational imaging tool, which has been thoroughly documented in a recent review.[19] In contrast, this paper focuses specifically on coherent nonlinear vibrational processes. Within this coherent domain, we summarize three representative systems: VSFG, CRS, and SBS, highlighting their underlying physical principles, key technological innovations, and recent applications across life sciences, materials science, and environmental science.

II. THEORETICAL FOUNDATIONS OF NONLINEAR VIBRATIONAL IMAGING

A. Nonlinear optical susceptibilities

Nonlinear optical effects originate from the energy exchange between interacting optical fields or between optical fields and materials. Both linear and nonlinear optical phenomena can be described by the interaction of the electric field component of light with the material system. As light propagates through a medium, the electric field E induces a macroscopic polarization P within the material, which is conventionally expressed as the sum of a linear and a nonlinear component $\mathrm{P} = \mathrm{P_L} + \mathrm{P_{NL}}$. In the linear regime, the induced polarization is directly proportional to the applied field and is given by $\mathrm{P_L} = \varepsilon_0 \boldsymbol{\chi}^{(1)} \mathrm{E}$, where $\boldsymbol{\chi}^{(1)}$ is the linear susceptibility, E is the electric field, and ε_0 is the vacuum permittivity.

In the nonlinear optical regime, achieved when the electric field intensity is sufficiently high—typically under focused laser excitation—the polarization response of the medium is no longer purely linear. This response is described by a power series expansion in the electric field strength

$$P = \varepsilon_0 \boldsymbol{\chi}^{(1)} E + \varepsilon_0 \boldsymbol{\chi}^{(2)} EE + \varepsilon_0 \boldsymbol{\chi}^{(3)} EEE + \cdots, \tag{1}$$

where $\boldsymbol{\chi}^{(2)}$ and $\boldsymbol{\chi}^{(3)}$ denote the second- and third-order nonlinear susceptibility tensors, respectively.

The optical electric field can be expressed as a discrete sum of its frequency components

$$\tilde{\boldsymbol{E}}(t) = \sum\nolimits_p \boldsymbol{E}(\omega_p) e^{i\omega_p t} + c.c. \tag{2}$$

Correspondingly, the nonlinear polarization induced in the medium can be written as

$$\tilde{\boldsymbol{P}}(r,t) = \sum\nolimits_n \boldsymbol{P}(\omega_p) e^{i\omega_p t}. \tag{3}$$

These frequency components in the polarization spectrum result from the nonlinear mixing of the input optical fields via the susceptibilities $\boldsymbol{\chi}^{(\mathrm{n})}$ $(\mathrm{n} \geq 2)$. This phenomenon underpins critical frequency-conversion processes, such as second-harmonic generation (SHG, $\boldsymbol{\chi}^{(2)}$), sum-frequency generation (SFG, $\boldsymbol{\chi}^{(2)}$), difference-frequency generation (DFG, $\boldsymbol{\chi}^{(2)}$), and four-wave mixing (FWM, $\boldsymbol{\chi}^{(3)}$).

We first consider the case of second-order nonlinear polarization. The general expression is given by

$$P_i^{(2)} = \varepsilon_0 \sum_{jk} \sum_{(pq)} \chi_{ijk}^{(2)}(\omega_\sigma, \omega_q, \omega_p) E_j(\omega_p) E_k(\omega_q), \quad (4)$$

where $\chi_{ijk}^{(2)}$ is the second-order susceptibility tensor and the indices i, j, k can each be x, y, or z polarization, ω_p and ω_q are frequencies of the incident fields, $\omega\sigma = \omega_p + \omega_q$ is the generated frequency. From time-dependent perturbation theory, the microscopic expression for $\chi_{ijk}^{(2)}$ is

$$\chi_{ijk}^{(2)}(\omega_\sigma, \omega_q, \omega_p) = \frac{N}{\epsilon_0 \hbar^2} \mathcal{P}_F \sum_{mn} \frac{\mu_{gn}^i \mu_{nm}^j \mu_{mg}^k}{(\omega_{ng} - \omega_\sigma)(\omega_{mg} - \omega_p)}, \quad (5)$$

where N is the molecular number density, $\mathcal{P}_F$ is full permutation operator for frequencies (ω_p, ω_q, and $-\omega_\sigma$) and $\mu_{ml} = \int u_m^* \hat{\mu} u_l \, d^3r$ is the transition dipole moment. The product of two transition dipole moments possesses the same symmetry properties as the Raman polarizability tensor.[18] And the triple product of dipole moments in Eq. (5) can be understood as a product of a dipole-allowed (IR-type) transition and a Raman-type transition.[18] As a third-rank tensor, $\chi_{ijk}^{(2)}$ governs all second-order nonlinear optical processes.

Next, we consider the third-order nonlinear polarization. Similarly, the third-order polarization can be expressed as

$$P_i^{(3)} = \varepsilon_0 \sum_{jkl} \sum_{(pqr)} \chi_{ijkl}^{(3)}(\omega_\sigma, \omega_r, \omega_q, \omega_p) E_j(\omega_p) E_k(\omega_q) E_l(\omega_r), \quad (6)$$

where the corresponding third-order susceptibility is given by

$$\chi_{ijkl}^{(3)}(\omega_\sigma, \omega r, \omega_q, \omega_p) = \frac{N}{\epsilon_0 \hbar^3} \mathcal{P}_F \sum_{mn\nu} \frac{\mu_{gv}^i \mu_{vn}^j \mu_{nm}^k \mu_{mg}^l}{(\omega_{vg} - \omega_\sigma)(\omega_{ng} - \omega_p - \omega_p)(\omega_{mg} - \omega_p)}. \quad (7)$$

Here, $\omega_\sigma = \omega_p + \omega_q + \omega_r$ and $\mathcal{P}_F$ denotes the full permutation operator over the input frequencies. For simplicity, we assume that the process of $\chi^{(3)}$ is parametric (implying no net energy exchange between the optical fields and the medium), though it also applies to nonparametric processes. The second-order nonlinear susceptibility $\chi^{(2)}$ typically exhibits a significantly larger magnitude than the third-order susceptibility $\chi^{(3)}$, even under off-resonant conditions. For instance, in quartz, the non-resonant $\chi^{(2)}$ is on the order of 10^{-9} esu, whereas $\chi^{(3)}$ is approximately 10^{-14} esu.

Our discussion of $\chi^{(2)}$ and $\chi^{(3)}$ thus far has been restricted to the non-resonant conditions. For resonant or near-resonant situations, the simple wave function expansion method based on the Schrödinger equation becomes inadequate. Instead, the density-matrix formalism must be employed to properly account for population dynamics. Given the complexity of this approach, we defer its treatment beyond the scope of this section.

B. Vibrational contrast mechanisms

Nonlinear vibrational microscopy techniques provide label-free image contrast by probing various coherent vibrational spectra. These methods selectively excite specific vibrational modes of materials to generate distinct optical signals. Crucially, the generated contrast depends on both vibrational frequencies and symmetry properties of the material system. (1) Second-order processes (e.g., VSFG) require non-centrosymmetric media and probe vibrations that are both IR- and Raman-active. This makes VSFG microscopy inherently sensitive to interfaces, oriented assemblies with asymmetric structures, and chiral molecules [Fig. 1(a)]. (2) Third-order processes probe Raman-active vibrations associated with polarizability modulations, primarily represented by coherent Raman scattering (CRS) microscopy, including coherent anti-Stokes Raman scattering (CARS), coherent Stokes Raman scattering (CSRS), and stimulated Raman scattering (SRS), as shown in Fig. 1(b). CRS microscopy is unique for its chemical specificity, capable of imaging bond vibrations of molecules and optical phonons in materials. (3) Stimulated Brillouin scattering (SBS) derives contrast from light–acoustic phonon interactions, where the Brillouin frequency shift directly reflects the sample's elastic modulus and viscoelasticity [Fig. 1(c)]. This enables SBS microscopy to map biomechanical properties in tissues and cells—complementing chemical contrast. Consequently, different species produce distinct spectral signatures, while signal intensity typically correlates with local concentration of targeted chemical groups. The complementary selection rules for different vibrational modes [Fig. 1(d)] using these imaging techniques enable comprehensive characterization of complex biological and materials systems. The contrast mechanism conditions for different processes are listed in Table I.

Nonlinear optical responses are intrinsically and highly sensitive to the local molecular environment. This sensitivity arises not only from the inherent polarizability of the molecules themselves but also from environmental influences on molecular arrangement, local field strength, and the extent of symmetry breaking, all of which can modify the effective $\chi^{(2)}$ or $\chi^{(3)}$ of the system.[21] As a second-order nonlinear process, VSFG is particularly sensitive to non-centrosymmetry. Consequently, in complex biological or material systems, the orientational order of molecules, hydrogen-bonding networks, surface charge, and local solvation structure can directly govern the signal intensity, peak positions, and spectral line shapes. For chiral interfaces, the symmetry of the system is reduced from $C_{\infty V}$ to C_∞. As a result, six additional nonlinear susceptibility tensor elements become nonzero: χ_{xyz}, χ_{yxz}, χ_{zxy}, χ_{zyx}, χ_{xzy}, and χ_{yzx}. By controlling the polarization states of light, these chiral signals can be effectively separated from non-chiral backgrounds.[22] In structurally ordered biological systems such as collagen fibers, different vibrational modes, including C–H and N–H stretching vibrations, possess transition dipole moments with distinct orientations; the coherent superposition of these modes can, therefore, give rise to characteristic interference patterns as the interfibrillar spacing varies.[23] By contrast, CRS more quantitatively reflects molecular concentration and local chemical compositions via hyperspectral imaging followed by spectral unmixing. Although in CARS, the dielectric properties of the surrounding medium and local field effects can generate a non-resonant background, yielding dispersive line shapes due to the interference between real and imaginary parts of $\chi^{(3)}$. In SBS, as a nonlinear optical process arises from the interaction between the incident field and the acoustic phonon field induced by electrostriction, the signal is fundamentally affected by factors including the chemical structure of the molecules, intermolecular interactions (hydrogen bonding and dipole–dipole forces), spatial organization, and the local thermodynamic state. These collectively govern material parameters such as the

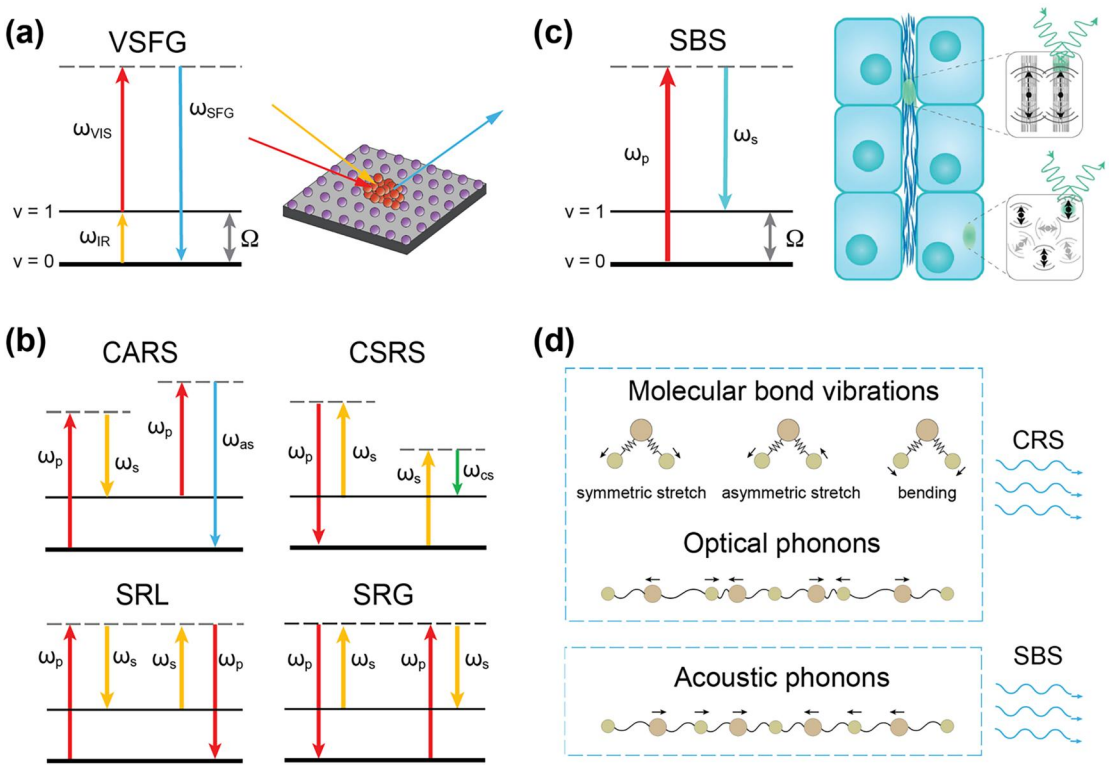

FIG. 1. Schematic diagrams of coherent vibrational transitions. (a) Vibrational sum-frequency generation (VSFG). (b) Coherent Raman scattering (CRS) processes, including coherent anti-Stokes Raman scattering (CARS), coherent Stokes Raman scattering (CSRS), stimulated Raman gain (SRG), and stimulated Raman loss (SRL). (c) Stimulated Brillouin scattering (SBS). Reproduced with permission from Prevedel *et al.*, Nat. Methods **16**, 969–977 (2019). Copyright 2019 Springer Nature.[186] (d) Comparison of vibrational modes for coherent Raman and Brillouin scattering.

refractive index, sound velocity, viscosity, and electrostrictive coefficient, which influence the linewidth and frequency shift of the SBS spectrum.

C. Phase-matching conditions

Phase matching is essentially the embodiment of the law of conservation of momentum in wave optics. When multiple optical fields of different frequencies propagate in a dispersive medium, the frequency dependence of the refractive index gives rise to distinct phase velocities. As a result, a phase mismatch can develop between the nonlinear polarization wave and the emitted signal wave. If this phase difference accumulates during propagation, destructive interference occurs, preventing efficient energy transfer from the fundamental light to the signal light. Therefore, phase matching requires the wave vectors $\vec{k}$ of all interacting waves to satisfy an appropriate vector relation so that constructive interference is maintained throughout the interaction volume.

As a second-order nonlinear process, VSFG requires a phase-matching condition to satisfy: $\vec{k}_{SFG} = \vec{k}_{vis} + \vec{k}_{IR}$. Owing to symmetry constraints, VSFG response is typically observed at interfaces and ordered structures where inversion symmetry is broken. As a third-order parametric process, CARS requires the wave-vector relation $\vec{k}_{as} = 2\vec{k}_p - \vec{k}_s$ to be satisfied. Although this condition can often be

TABLE I. Comparisons between different nonlinear coherent vibrational microscopy modalities.

	VSFG	CRS	SBS
Contrast mechanism	Non-centrosymmetry, interfaces, chirality	Chemical bond vibrations, optical phonons	Acoustic phonons
Spatial resolution	∼1 μm[44]	∼300 nm (near-infrared), 86 nm (visible)[113]	490 nm[185]
Sensitivity	Sub-monolayer[34]	∼mM (usual), single molecule (electronic resonance)[114]	Not specified
Penetration depth	Not specified	∼200 μm (usual), ∼1 mm (tissue clearing)[129]	Not specified
Imaging speed	∼1 s/frame[37]	Video rate[91]	∼1 min/frame[185]

fulfilled through tight focusing or suitable beam geometries, the generated signal remains susceptible to coherent interference from the non-resonant background. By contrast, SRS is often regarded as effectively self-phase-matched because the signal field appears to have the same wave vector and frequency as one of the incident beams; thus, the participating fields remain intrinsically phase synchronized in space. This is one reason SRS can provide spectra largely free of the non-resonant background. Finally, in SBS, phase matching involves momentum exchange between photons and acoustic phonons, described by $\vec{k}_p = \vec{k}_s + \vec{q}$. This process satisfies a Bragg-like condition through a moving grating induced by electrostriction, and both the matching efficiency and the associated frequency shift are directly linked to the viscoelastic properties of the medium.

D. The focusing characteristics

In nonlinear optical microscopy, the focusing characteristics of light beams are fundamental factors determining the efficiency of light–matter interaction, spatial resolution, and the signal-to-noise ratio. Depending on physical constraints and propagation geometry, light fields are typically classified into two basic states: tightly focused and loosely focused. Tight focusing refers to light being focused by a high numerical aperture (typically NA >0.7) lens system, producing a sub-wavelength spatially confined field at the focal region. In this state, the large angle between the wave propagation direction and the optical axis renders the conventional paraxial approximation no longer applicable. In contrast, loosely focused fields, which are common in traditional far-field spectroscopy, follow scalar diffraction laws under the paraxial approximation.[24]

The Richards–Wolf formalism serves as the most authoritative mathematical framework for describing tightly focused light fields. Based on the Debye approximation, this theory treats the electric field strength E_f near the focus as a coherent superposition of plane waves from all incident directions,

$$E_f(x,y,z) = \frac{ikfe^{ikf}}{2\pi}\int_{\phi=0}^{2\pi}\int_{\theta=0}^{\theta_{max}} E_{far}(\theta,\phi) \times e^{ik(x\sin\theta\cos\phi + y\sin\theta\sin\phi + z\cos\theta)}\sin\theta d\theta d\phi, \quad (8)$$

where E_{far} is the incoming far field, f denotes the focal length of the focusing lens, k is wave vectors and θ_{max} is the maximum angle of the resulting light cone. For a typical tightly focused system, the total electric field at the focus no longer contains only transverse components but also exhibits a significant longitudinal electric field component parallel to the optical axis. Tightly focusing can compress the sampling volume to the extreme, enabling the system to achieve a diffraction-limited resolution of 200–300 nm.

Under tightly focused conditions, because the interaction volume is confined to a submicrometer scale, the phase-matching conditions are significantly relaxed. This localized relaxation enables backward radiation (epi-detection), particularly for particles smaller than the wavelength (such as lipid droplets), which cannot be achieved in loosely focused systems. Tight focusing not only determines spatial resolution but also dictates the excitation efficiency of nonlinear processes. Because tight focusing generates extremely high local power density (irradiance), nonlinear excitation occurs only within a minute focal volume, granting the microscope excellent depth-sectioning capabilities.[25] Furthermore, tight focusing can effectively eliminate ensemble averaging effects, thereby enabling the detection of single-molecule dynamics, structural fluctuations, or local chemical heterogeneity at the nanoscale.[26]

Another important feature of tight focusing is the Gouy phase shift, resulting in a full π-phase swing along the optical axis near the focal region. It is a consequence of the spatial confinement of the field in the lateral dimension in real space, while it ensures that all the **k** components of the wavefront remain in phase upon traversing the focal region. This phenomenon plays an important role in coherent optical microscopies. In particular, Gouy phase mismatch is especially prominent in four-wave mixing processes, such as third-harmonic generation (THG), in which it strongly affects the spatial distribution of the emitted third-order signal and automatically suppresses background noise. However, in CRS processes such as CARS, the phase mismatch remains small within the interaction volume and hence is not largely affected by the Gouy phase shift.

III. SUM-FREQUENCY GENERATION (SFG) MICROSCOPY

SFG is a second-order nonlinear optical process occurring exclusively in non-centrosymmetric media or interfaces. A special case is second harmonic generation (SHG), where identical input frequencies ($\omega_1 = \omega_2$) produce $2\omega_1$ output. While both SFG and SHG arise from $\chi^{(2)}$, SFG extends the capabilities by incorporating vibrational selectivity through infrared resonance, enabling molecular-specific characterization, known as VSFG.[27] In a typical VSFG experiment, spatially and temporally overlapped beams—a fixed visible/near-infrared beam and a tunable mid-infrared beam—interact within the medium. When the frequency of the IR beam matches the vibrational mode of interfacial molecules, the generated signal at the sum frequency ($\omega_{SFG} = \omega_1 + \omega_2$) is strongly enhanced [Fig. 1(a)], producing a vibrationally resonant spectrum that reflects the chemical composition and orientational order of the interface. The nonlinear polarization $\chi^{(2)}(\omega_3; \omega_1, \omega_2)$ consists of a non-resonant background determined by the dielectric properties of the material and a resonant contribution amplified upon vibrational matching. This resonant amplification provides the high vibrational sensitivity while maintaining interface/symmetry specificity, enabling simultaneous detection of non-vanishing $\chi^{(2)}$ and molecular bond vibrations.

SFG requires non-vanishing $\chi^{(2)}$, which vanishes in bulk isotropic media (gases/liquids) due to inversion symmetry. Symmetry breaking at interfaces between such phases produces nonzero $\chi^{(2)}$, this intrinsic surface sensitivity established VSFG as a powerful interfacial spectroscopic tool. Historically applied to planar interfaces, revealing molecular orientation, ordering, and dynamics at interfaces—notably mapping water-network structures through OH-stretch vibrations and characterizing phospholipid headgroups at membranes. The vibrational contrast of VSFG further enables microscopic imaging by integrating structural sensitivity with chemical specificity. Unlike conventional non-resonant SHG, VSFG simultaneously probes symmetry breaking and molecular conformations via mid-IR resonance. With submicrometer resolution and inherent symmetry selectivity, it effectively characterizes molecular films, chiral crystals, and biological fibrillar structures lacking centrosymmetry. Ongoing advances in light sources and optical components will continue to expand VSFG microscopy's vital role in biology and materials science.

A. Development of SFG microscope

The transition of SFG from spectroscopy to imaging began with Flörsheimer *et al.* in their 1999 demonstration [Fig. 2(a)],[28] which employed total internal reflection through a prism to separate the SFG signal detected via a polarization microscope and an intensified charge-coupled device (ICCD). This initial approach suffered from limited magnification and numerical aperture (NA) due to the oblique signal emission requiring large depth-of-focus objectives. Subsequent innovations addressed these constraints: Hoffmann *et al.* enhanced signal intensity in opaque/reflective samples using ∼60° oblique illumination, implementing a blazed grating for distortion-free imaging and four-stage optical filtering to achieve background suppression.[29] Further refinements came from Kuhnke *et al.* in achieving molecule-specific imaging of chemically patterned monolayers[30] and Mizutani *et al.* in combining polarization-resolved excitation with narrowband filters to reach 2.2 μm resolution [Fig. 2(b)].[31] Optical configurations evolved significantly with Locharoenrat *et al.*'s 2009 confocal SFG microscope,[32] where wide-field IR illumination combined with focused visible excitation through high-NA objectives improved optical sectioning and axial resolution. Inoue *et al.* then developed a non-scanning wide-field vibrational SFG microscope (2010) using coaxial beams for full-field illumination (∼100 μm area) and ICCD detection,[33] substantially increasing imaging speed while minimizing photodamage.

Imaging speed advanced markedly through computational and laser innovations. Cai *et al.* introduced compressed sensing using Digital Micromirror Device (DMD) pattern projection and photomultiplier tube (PMT) detection,[34] later extending this to compressive broadband hyperspectral SFG imaging for simultaneous spatial–spectral reconstruction.[35] Concurrently, Raghunathan *et al.* demonstrated a fast vibrational SFG microscope with ∼0.6 μm resolution at ∼1-min per 256 × 256 pixel image using a high-repetition-rate (76 MHz) picosecond optical parametric oscillator (OPO) laser with collinear excitation [Fig. 2(c)].[36] This group subsequently integrated SFG with coherent anti-Stokes Raman scattering (CARS), third-order sum-frequency generation (TSFG), and two-photon fluorescence (TPF) for multimodal imaging at ∼1 frame/s.[37]

Molecular orientation and chirality probing progressed through several key developments: In 2006, Ji *et al.* developed a three-dimensional chiral SFG microscope, enabling electric-dipole-allowed chiral visualization [Fig. 2(d)].[38] In 2013, Han *et al.* introduced phase-sensitive vibrational resonance sum-frequency generation (PSVSFG) microscopy with interferometric detection to retrieve the phase information of $\chi^{(2)}$ for polarity orientation mapping in biological samples [Fig. 2(e)],[39] later adding polarization resolution to separate $\chi^{(2)}$ tensor components for collagen imaging.[40] In 2017, Wang *et al.* proposed a self-phase-stabilized heterodyne detected SFG (HD-SFG) microscope using all-collinear geometry to achieve ninefold enhanced phase stability for submicrometer orientation/conformation distinction.[41] Most recently (2024), Ji *et al.* demonstrated diffraction-limited chiral imaging using radially polarized vector beams in collinear geometry.[42]

Computational integration accelerated in 2020 when Shah and Baldelli combined compressed sensing, target factor analysis, and neural networks to enhance the speed and chemical interpretability of SFG imaging.[43] Wagner *et al.* then developed a fast line-scan vibrational hyperspectral SFG microscopy with neural networks, extracting molecular orientation and tilt angles in self-assembled molecular monolayers.[44]

B. Applications

1. Interfaces and self-assembled structures

SFG microscopy provides label-free visualization of interfacial molecular organization and non-centrosymmetric assemblies through vibrational-selective imaging. By probing molecular vibrations (e.g., C–H stretching), it resolves molecular orientation, distribution, and local chemical environments at surfaces with micrometer resolution. Fang and Baldelli demonstrated this capability by imaging octadecanethiol monolayers on copper, revealing how surface anisotropy influences molecular packing through signal variations across crystal grains.[45] This technique offers critical insights for molecular electronics, catalysis, and material design. Wang *et al.* further advanced dynamical studies by combining pump–probe spectroscopy with VSFG imaging within single self-assembled domains (∼1 μm), distinguishing hydrogen-bonding dynamics of primary and secondary hydroxyl groups in β-cyclodextrin.[46] Their discovery of hydration heterogeneity between domains provided a mechanistic basis for understanding flexibility in biomimetic lattice materials.

2. Life sciences

a. Tissue imaging. SFG microscopy enables label-free mapping of extracellular matrix architecture through vibrationally resolved collagen-I imaging. It quantifies fibril orientation, interfibrillar spacing, and molecular order across wide fields of view.[40,47] Hyperspectral implementations enhance throughput and specificity for tissue-scale surveys of heterogeneous collagen organization.[36,37,48] Most recently, Yang *et al.* employed high-speed line-scan SFG to image lung tissue, identifying 10- to 20-fold enhancements in NH/CH_2 and CH/CH_2 symmetric-stretch intensity ratios as robust tumor spectral markers [Fig. 2(f)].[23]

b. Lipid membranes. SFG microscopy quantifies phospholipid organization and phase transformations at interfaces with spatial resolution. Compressive-sensing SFG microscopy revealed micrometer-scale phase separation in DSPC/DLPC monolayers at air–water interfaces, demonstrating molecular exchange between liquid-condensed and liquid-expanded phases.[49] Fellows *et al.* achieved comprehensive characterization using complementary approaches: Azimuthal-scanned SFG mapped density and 3D orientation variations, identifying boundary rims with reduced density and in-plane order, while phase-resolved SFG on mixed-chirality membranes revealed chirality-dependent spiraling packing and enantio-selective domain growth [Fig. 2(g)].[50,51]

IV. COHERENT RAMAN SCATTERING (CRS) MICROSCOPY

A. Principles

CRS encompasses third-order nonlinear optical processes where synchronized pump (ω_p) and Stokes (ω_s) beams coherently excite molecular vibrations. When the frequency difference between the two beams ($\omega_p - \omega_s$) matches vibrational resonance Ω, a third-order polarization is enhanced to generate coherent optical emission. Under

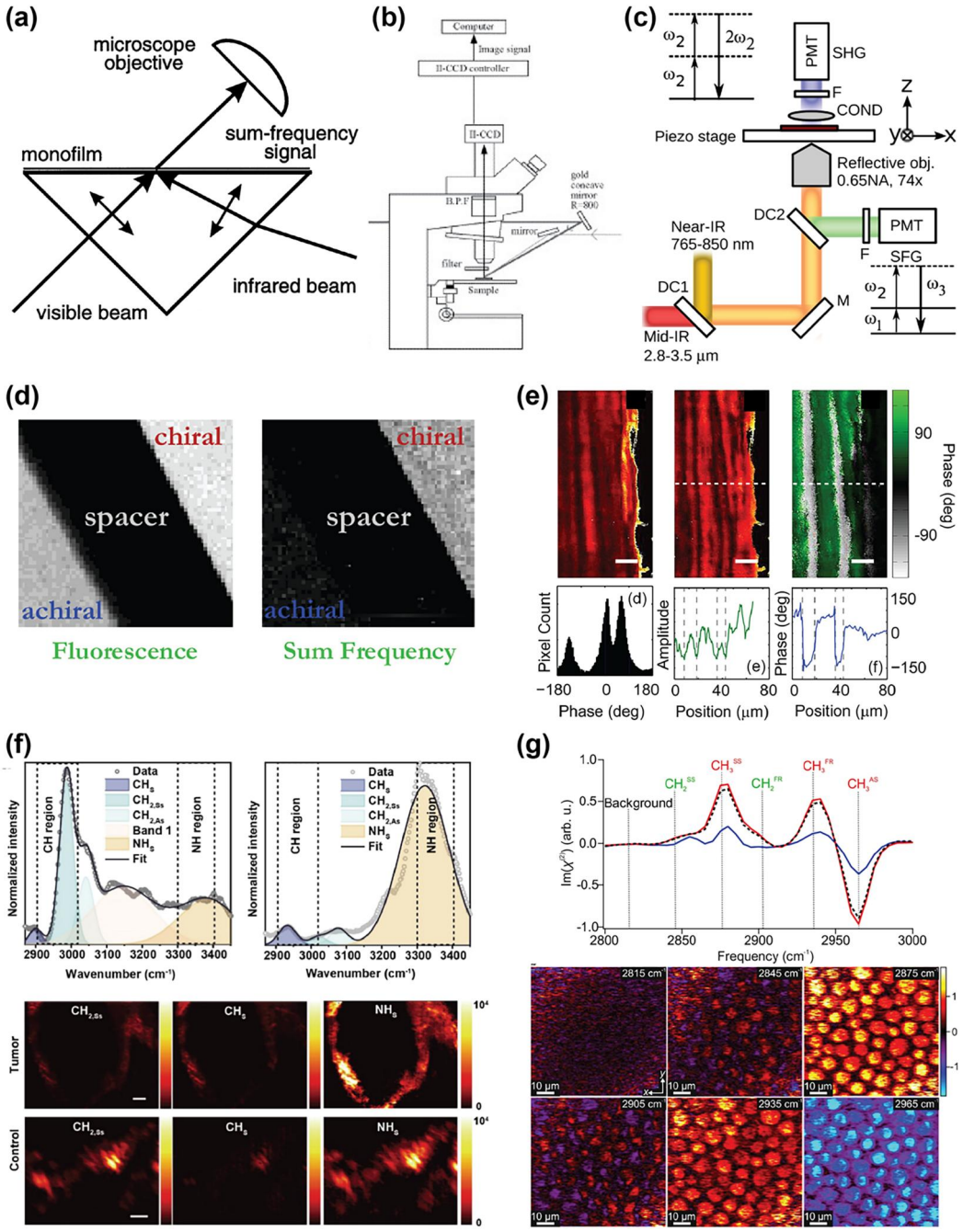

FIG. 2. Developments and applications of SFG microscopy. (a) The first SFG imaging system used total internal reflection through a prism to separate the weak SFG signal. Reproduced with permission from Flörsheimer *et al.*, Langmuir **15**, 5437–5439 (1999). Copyright 1999 American Chemical Society.[28] (b) SFG microscope combining polarization-resolved infrared and visible excitation with narrowband filters and a time-gated image intensifier CCD. Reproduced with permission from Mizutani *et al.*, Spectrochim. Acta, Part A **62**, 845–849 (2005). Copyright 2005 Elsevier B.V.[31] (c) Fast vibrational SFG microscope using a high-repetition-rate (76 MHz) picosecond OPO laser through a collinear optical path. Reproduced with permission from Raghunathan *et al.*, Opt. Lett. **36**, 3891–3893 (2011). Copyright 2011 Optica Publishing Group.[36] (d) Fluorescence image and SFG image of a racemic BINOL solution measured with SPP polarization combination by Ji in 2006. Reproduced with permission from Ji *et al.*, J. Am. Chem. Soc. **128**, 3482–3483 (2006). Copyright 2006 American Chemical Society.[38] (e) VSFG images of rat tail tendon tissue on top of z-cut quartz. Reproduced with permission from Han *et al.*, J. Phys. Chem. B **117**, 6149–6156 (2013). Copyright 2013 American Chemical Society.[39] (f) VSFG spectra and images of control and tumor tissues. Reproduced with permission from Yang *et al.*, J. Am. Chem. Soc. **147**, 36657–36668 (2025). Copyright 2025 American Chemical Society.[23] (g) SFG spectra and images of the (R)-DPPC/(R)-POPC monolayer at select frequencies. Reproduced with permission from Fellows *et al.*, Nat. Commun. **15**, 3161 (2024). Copyright 2024 Springer Nature.[51]

phase-matching conditions, resonant vibrations are driven coherently and in phase, leading to directional, high-intensity emission with several orders of magnitude (typically 10^3–10^4 times) enhancement compared to non-resonant processes.

Key CRS signals include coherent anti-Stokes Raman scattering (CARS) at $\omega_{as} = 2\omega_p - \omega_s$; coherent Stokes Raman scattering (CSRS) at $\omega_{cs} = 2\omega_s - \omega_p$; and stimulated Raman scattering (SRS) with stimulated Raman gain (SRG) and loss (SRL) detected at ω_s and ω_p, respectively. The corresponding energy diagrams are illustrated in Fig. 1(b). These signals all arise simultaneously from the same Raman-active vibrational transition and can be discriminated experimentally through spectral filtering or modulation schemes, providing vibrational-specific contrast for label-free chemical imaging.

Unlike spontaneous Raman scattering—limited by weak scattering cross section and long integration times—CRS employs coherent excitation to boost signal intensity through third-order nonlinear interactions. This enables rapid, high-sensitivity imaging while preserving chemical specificity.

1. Coherent anti-Stokes Raman scattering (CARS)

Formally, the nonlinear CARS polarization can be expressed as $P(\omega_{as}) = 3\varepsilon_0\chi_R^{(3)}(\omega_{as})E_s|E_p|^2e^{i(2k_p-k_s)z}$, where ε_0 is the vacuum permittivity. These induced polarizations generate coherent fields in a medium with length L that give rise to an anti-Stokes signal, which can be expressed as

$$I_{CARS} \propto \left|\chi^{(3)}(\omega_{as})\right|^2 |I_p|^2|I_s|^2L^2\sin c^2\left(\frac{\Delta kL}{2}\right). \quad (9)$$

For this, the anti-Stokes field must be in phase with the induced nonlinear polarization for every point along the z-axis. This is what is known as the "phase-matching condition" that requires $\Delta k = 2k_p - k_s - k_{as} = 0$.

In the CARS process, the frequency difference between the pump and Stokes beams ($\omega_p - \omega_s$) matches a molecular vibrational frequency Ω. This vibration is then probed by the pump pulse, generating an anti-Stokes signal at $\omega_{as} = 2\omega_p - \omega_s$. As a four-wave mixing (FWM) process, CARS can also produce a signal through a non-resonant pathway, where the beams interact only with the instantaneous electronic response of the medium rather than with a specific molecular vibration. The total CARS susceptibility can be written as the sum of the resonant and non-resonant components $\chi^{(3)} = \chi_R^{(3)} + \chi_{NR}^{(3)}$. Introducing this expression in Formula (8), the CARS signal can be expressed as

$$I_{CARS} \propto \left|\chi_R^{(3)} + \chi_{NR}^{(3)}\right|^2 \propto \left|\chi_R^{(3)}\right|^2 + \left|\chi_{NR}^{(3)}\right|^2 + 2\chi_{NR}^{(3)}Re\left[\chi_R^{(3)}\right]. \quad (10)$$

This non-resonant contribution is near constant in the spectral domain and interferes with the real (dispersive) part of the resonant susceptibility, resulting in off-resonant background and distorted spectra of CARS.

2. Coherent Stokes Raman scattering (CSRS)

In the CSRS process, the first interaction of the pump and Stokes beams establishes a vibrational coherence with a frequency of $\Omega = \omega_1 - \omega_2$ like that in CARS. This coherence is then read out by another interaction of the Stokes beam (ω_2), resulting in the emission of a Stokes photon. The signal frequency and phase-matching condition are determined by energy and momentum conservation, respectively: $\omega_{CSRS} = 2\omega_2 - \omega_1$, $k_{CSRS} = 2k_2 - k_1$. The emitted CSRS signal lies on the red-shifted side of the spectrum. Under accessible electronic resonance conditions, it is, therefore, more susceptible to resonance enhancement but also more prone to spectral overlap with the excitation Stokes beam and to fluorescence interference.

3. Stimulated Raman scattering (SRS)

SRS process occurs simultaneously with CARS and CSRS but does not generate photons with new frequencies. Instead, SRS induces third-order nonlinear polarizations at the same frequencies as the excitation beams: $P(\omega_P) = 6\varepsilon_0\chi_R^{(3)}(\Omega)E_p|E_s|^2$ and $P(\omega_s) = 6\varepsilon_0\chi_R^{(3)} \times(-\Omega)E_s|E_p|^2$. These induced polarizations generate coherent electric fields that interfere with the corresponding input beams, giving rise to stimulated Raman loss (SRL) in the pump beam and stimulated Raman gain (SRG) in the Stokes beam. SRS signal is detected as the differential intensity change as

$$\Delta I_{SRG} \propto Im\left[\chi_R^{(3)}(\Omega)\right]|E_p|^2|E_s|^2, \quad (11)$$

$$\Delta I_{SRL} \propto -Im\left[\chi_R^{(3)}(\Omega)\right]|E_p|^2|E_s|^2, \quad (12)$$

where the imaginary part of $\chi_R^{(3)}(\Omega)$ represents the dissipative vibrational response. Since $Im[\chi_R^{(3)}(\Omega)]$ is linearly proportional to both the molecular number density (N) and the Raman scattering cross section (σ_{Raman}), the intensity changes can be approximated as $\Delta I_{SRL} \propto N\sigma_{Raman}I_pI_s$, $\Delta I_{SRG} \propto -N\sigma_{Raman}I_pI_s$. This linear relationship between the SRS signal and molecular concentration enables quantitative chemical mapping of the sample. By tuning the frequency difference between the pump and Stokes beams to match specific vibrational resonances, SRS microscopy provides molecularly specific contrast, allowing detailed chemical mapping of heterogeneous samples based on well-characterized Raman vibrational spectra.[24]

Unlike CARS and CSRS, photon energy is no longer conserved in SRS. During the SRS process, a portion of pump photons is annihilated, generating an equal number of Stokes photons, with the loss of photon energy transferred to the molecular system as vibrational excited states.[52] Since the non-resonant $\chi_{NR}^{(3)}(\Omega)$ is nearly real, SRS signals are essentially free from non-resonant background. Moreover, SRS preserves the vibrational spectra of spontaneous Raman scattering due to its proportionality to $Im[\chi_R^{(3)}(\Omega)]$.

B. CARS microscopy

1. Instrumental developments

a. Non-collinear scheme to collinear geometry. Duncan *et al.* first demonstrated a non-collinear CARS microscope using visible excitation with stringent phase-matching requirements, yielding a strong non-resonant background.[53] Zumbusch *et al.* revolutionized the field in 1999 by developing a collinear CARS microscopy system with high-NA objectives, relaxing phase-matching constraints while providing optical sectioning and reduced photodamage through near-IR (NIR) excitation [Fig. 3(a)].[54]

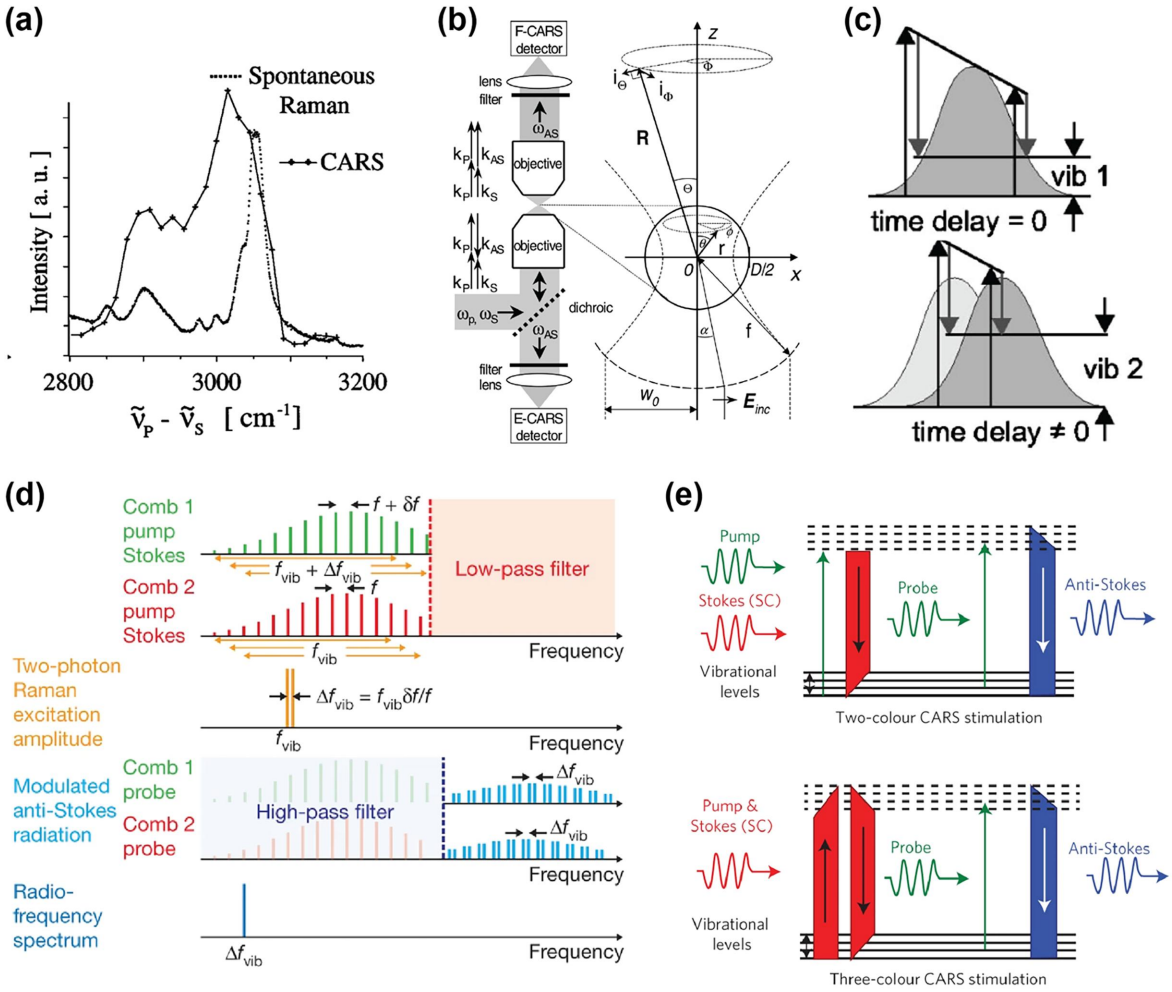

FIG. 3. Developments of CARS microscopy. (a) CARS spectrum of a 910 nm diameter polystyrene bead. Reproduced with permission from Zumbusch *et al.*, Phys. Rev. Lett. **82**, 4142–4145 (1999). Copyright 1999 American Physical Society.[54] (b) Schematic of the configurations for F- and E-CARS microscopy with collinear pump and Stokes beams and confocal detection in the forward and backward directions, respectively. Reproduced with permission from Volkmer *et al.*, Phys. Rev. Lett. **87**, 023901 (2001). Copyright 2001 American Physical Society.[56] (c) Schematic of CARS microscope combined with spectral focusing techniques. Reproduced with permission from Hellerer *et al.*, Appl. Phys. Lett. **85**, 25–27 (2004). Copyright 2004 AIP Publishing LLC.[62] (d) Dual-comb CARS using two frequency combs to modulate the excitation of molecular vibration with the difference frequency Δf_{vib}. This modulation is then transferred by the combs to the anti-Stokes radiation. Reproduced with permission from Ideguchi *et al.*, Nature **502**, 355–358 (2013). Copyright 2013 Springer Nature.[64] (e) Schematic of the BCARS CRI system. Reproduced with permission from Charles *et al.*, Nat. Photonics **8**, 627–634 (2014). Copyright 2014 Springer Nature.[65] (f) Super-resolution HO-CARS images of live unstained buccal cells. Reproduced with permission from Gong *et al.*, Nat. Photonics **14**, 115–122 (2020). Copyright 2020 Springer Nature.[73]

b. Epi-detection. In 2001, Cheng *et al.*[55] and Volkmer *et al.*[55,56] introduced picosecond NIR pulses with backward detection, demonstrating comparable forward/epi-CARS signals for small scatterers or thin samples because of the phase-matching conditions [Fig. 3(b)]. This finding established epi-detected CARS (e-CARS) as an effective approach for background suppression and enhanced detection sensitivity in biological specimens. Evans *et al.* extended epi-CARS to thick tissues by detecting backscattered forward-propagating CARS signals, achieving video-rate (20 fps) live skin imaging.[57]

c. Multiplexing. While picosecond single-color CARS provides high temporal and spectral resolutions, a single detection frequency lacks chemical resolution. Therefore, early single-color systems gave way to multiplex approaches: (1) Two-color broadband CARS (BCARS, 2002) combining a narrowband picosecond pump pulse with a broadband femtosecond Stokes pulse to acquire CARS spectra spanning hundreds of wavenumbers.[58–60] In this configuration, the narrowband pump defines the spectral resolution, while the femtosecond Stokes pulse determines the spectral coverage. (2) Time-resolved CARS introduced by Volkmer *et al.* employing three femtosecond lasers—one for signal detection and two for exciting multiple vibrational modes—with the CARS spectrum reconstructed via Fourier transform.[61] (3) Spectral-focusing CARS approach implemented by Hellerer *et al.* using chirped pulses (from femtosecond to picosecond) to achieve rapid frequency tuning (via time-delay scanning) without changing laser wavelengths [Fig. 3(c)].[62] (4) Fourier-transform CARS developed by Ogilvie *et al.* using a single broadband laser combined with a Michelson interferometer, enabling broadband imaging across 1500 cm^{-1}.[63] To improve temporal scanning speed, Ideguchi *et al.* utilized two laser frequency combs to acquire broad spectral components with microsecond acquisition time and high spectral resolution [Fig. 3(d)].[64] (5) Three-color broadband CARS (BCARS) was introduced by Charles *et al.* based on intrapulse three-color excitation, exploiting the non-resonant background to enhance weak fingerprint vibrations [Fig. 3(e)].[65] They used tailored co-seeded fiber lasers to generate a narrowband flat-top probe (770 nm; ∼16 mW, 3.4 ps pulses on-sample) and a supercontinuum (SC: ∼900 to 1350 nm; ∼9.5 mW, ∼16 fs pulses on-sample) with negligible jitter.

d. Widefield CARS. While most CARS microscopes adopt laser-scanning configurations, widefield geometry is expected to gain imaging speed and throughput. Heinrich *et al.* employed a dark-field condenser to deliver two pump beams at large incident angles and a coaxial Stokes beam through the objective, achieving geometric phase matching across the full field of view and enabling parallel detection of the anti-Stokes signal using a charge-coupled device (CCD) camera.[66] Since then, different excitation strategies for wide-field CARS have emerged. Toytman *et al.* demonstrated non-phase-matching illumination to realize simultaneous imaging of extended regions.[67] Heinrich *et al.* enhanced axial resolution and optical sectioning by incorporating dynamic speckle illumination.[68] Lei *et al.* proposed collinear non-phase-matching illumination by defocusing pump and Stokes beams onto the sample.[69] Berto *et al.* used wavefront sensing to retrieve both resonant and non-resonant components without a reference beam.[70] More recently, Zong *et al.* developed wide-field surface-enhanced CARS (WISE-CARS), achieving ultrafast hyperspectral imaging at 120 frames/s over a 130 × 130 μm^2 field of view via spectral-focusing.[71] Fantuzzi *et al.* introduced CARS-RIM, which combined random illumination to achieve 3 μm axial resolution and 300 nm lateral resolution.[72] This configuration used a high-power, high-repetition-rate laser to get strong nonlinear excitation (a Yb-based amplified solid-state laser split into two parts as the Stokes and pump beams) and combined it with random illumination, effectively reducing the peak excitation intensity on the sample, although image acquisition remained relatively time-consuming.

e. Higher-order CARS. Gong *et al.* proposed higher-order CARS (HO-CARS),[73] demonstrating higher-order nonlinearity under tight focusing, including $\chi^{(5)}$ [six-wave mixing (SWM), $\omega_{SWM} = 3\omega_p - 2\omega_s$] and $\chi^{(7)}$ [eight-wave mixing (EWM), $\omega_{EWM} = 4\omega_p - 3\omega_s$]. These higher-order signals positioned away from the conventional CARS band can be detected with a lower non-resonant background and provide enhanced 3D resolution [Fig. 3(f)].

2. Applications

a. Cell imaging. CARS microscopy enables label-free chemical imaging of cellular components through sensitive detection of C–H vibrational signatures, revealing distributions of lipids, proteins, and other biomolecules. Nan *et al.* tracked neutral lipid droplet dynamics in live fibroblasts, observing depletion during early differentiation followed by reaccumulation.[74] Subsequent work by Paar *et al.* elucidated lipid droplet metabolism during lipolysis, demonstrating growth via inter-organelle lipid transfer [Fig. 4(a)].[75] In oncology, Le *et al.* monitored diet-dependent metastatic behavior in cancer models,[76] while Mitra *et al.* distinguished circulating tumor cells from leukocytes based on significantly elevated CARS signals in prostate cancer.[77] Molecular transport studies include Okuno *et al.*'s quantification of surfactant accumulation across endosomal and membrane systems.[78] For lipid metabolism, Di Napoli *et al.* implemented dual-frequency CARS to quantify saturated and unsaturated lipid distributions in human adipose-derived stem cells.[79]

b. Tissue imaging. The label-free capabilities of CARS microscopy facilitate chemical imaging of intact tissues, particularly in neurological and pathological contexts. Huff and Cheng demonstrated *in vivo* CARS imaging of myelin sheaths in rat sciatic nerves, revealing perineuronal adipocytes' contrast through 3D imaging.[80] Shi *et al.* achieved continuous *in vivo* imaging in spinal cords, resolving myelin structures, axons, and Ranvier nodes.[81] In vascular disease research, Wang *et al.* combined CARS with other nonlinear modalities to classify atherosclerotic plaques and quantify collagen/lipid contents within plaques,[82] with complementary studies by Lim *et al.*[83] and Mostaço-Guidolin *et al.*[84] identifying cholesterol crystals. For clinical diagnostics, Kiss *et al.* performed staining-free histopathological imaging of basal cell carcinoma using dual-frequency CARS,[85] Charles *et al.* applied a broadband CARS system to enable 3D chemical imaging of DNA, collagen, proteins, and lipids in mouse pancreatic tissues,[65] while Chen *et al.* characterized lipid granule diversity in live nematodes [Fig. 4(b)].[86] Clinically relevant advances include real-time endoscopic assessment of inflammatory bowel disease using multimodal CARS/TPEF/SHG imaging [Fig. 4(c)].[87]

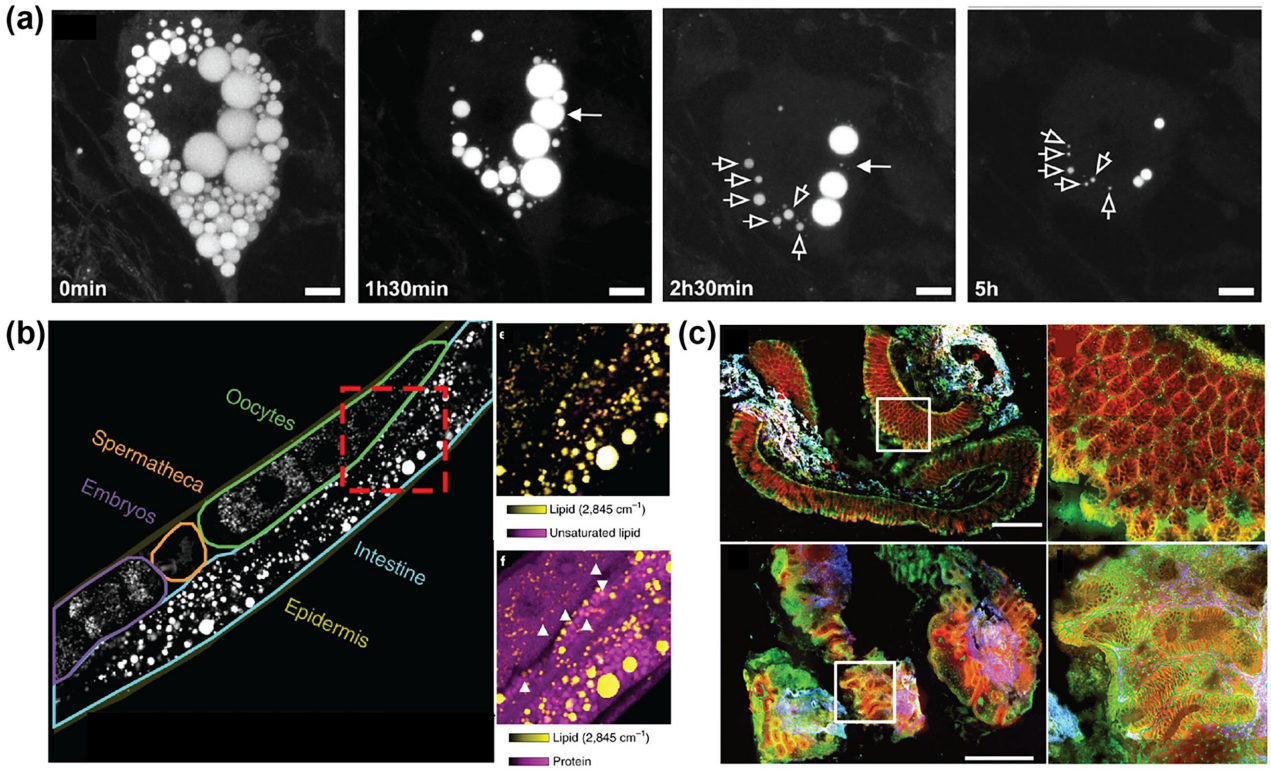

FIG. 4. Applications of CARS microscopy. (a) Depletion of neutral lipid stores in 3T3-L1 adipocytes. Reproduced with permission from Paar *et al.*, J. Biol. Chem. **287**, 11164–11173 (2012). Copyright 2012 Elsevier B.V.[75] (b) Distinct chemical features of lipid-rich particles in *C. elegans*. Reproduced with permission from Chen *et al.*, Nat. Chem. Biol. **16**, 1087–1095 (2020). Copyright 2020 Springer Nature.[86] (c) Multimodal images with the combination of CARS, TPEF, and SHG. Reproduced with permission from Chernavskaia *et al.*, Sci. Rep. **6**, 29239 (2016). Copyright 2016 Springer Nature.[87]

c. Materials science. CARS microscopy provides rapid, bond-specific tomography for materials characterization due to its optical sectioning capability and vibrational sensitivity. von Vacano *et al.* employed multiplex CARS to image ternary polymer blends (PS/PET/PMMA), distinguishing material phases and reconstructing virtual cross sections of adhesive layers.[88] In catalysis research, Kox *et al.* mapped heterogeneous thiophene distributions within zeolite crystals (H-ZSM-5), revealing diffusion-limiting effects during conversion reactions through 2D chemical imaging.[89]

C. CSRS microscopy

In 2023, Heuke and Rigneault[90] achieved the first demonstration of CSRS microscopic imaging under laser-scanning conditions [Fig. 5(a)]. In biomedical specimens, the CSRS signal is often strongly obscured by intense linear fluorescence. Conventional suppression approaches—such as time-gated detection, streak camera-based time-resolved imaging, or polarization filtering—typically require substantial modifications to the microscope setup or exhibit limited effectiveness in highly fluorescent environments. To address this challenge, the authors proposed two new fluorescence suppression strategies: (1) Spectral filtering based on the intrinsically narrow bandwidth of CSRS under picosecond excitation. By combining two bandpass filters with different central wavelengths and tilting them to fine-tune the transmission window, they achieved a narrow spectral passband of <3 nm, effectively removing most fluorescence background [Fig. 5(b)]. (2) Dual-beam modulation and demodulation. The pump and Stokes beams were modulated at distinct frequencies (f1 and f2), and the detected signal was demodulated at either $f1 - f2$ or $f1 + f2$ [Fig. 5(c)], isolating nonlinear signals that depend simultaneously on both beams and thus separating the CSRS response from single-color two-photon fluorescence. Using visible excitation wavelengths of 445 nm (pump) and 515 nm (Stokes), the authors demonstrated that even in the visible regime, where fluorescence artifacts are typically more severe, it is possible to obtain pure, background-free CSRS signals. This establishes the feasibility of extending CSRS imaging to deep-tissue applications in the near-infrared region [Fig. 5(d)].

D. SRS microscopy

1. Instrumental developments

SRS microscopy was developed as a solution to the persistent non-resonant background that limited CARS imaging.[91] Ploetz *et al.* demonstrated the first femtosecond SRS imaging using a low-repetition-rate femtosecond laser system, acquiring Raman images through raster scanning.[92] Xie's group introduced the SRS microscope based on high-repetition-rate picosecond lasers coupled with high-frequency phase-sensitive detection, which markedly enhanced

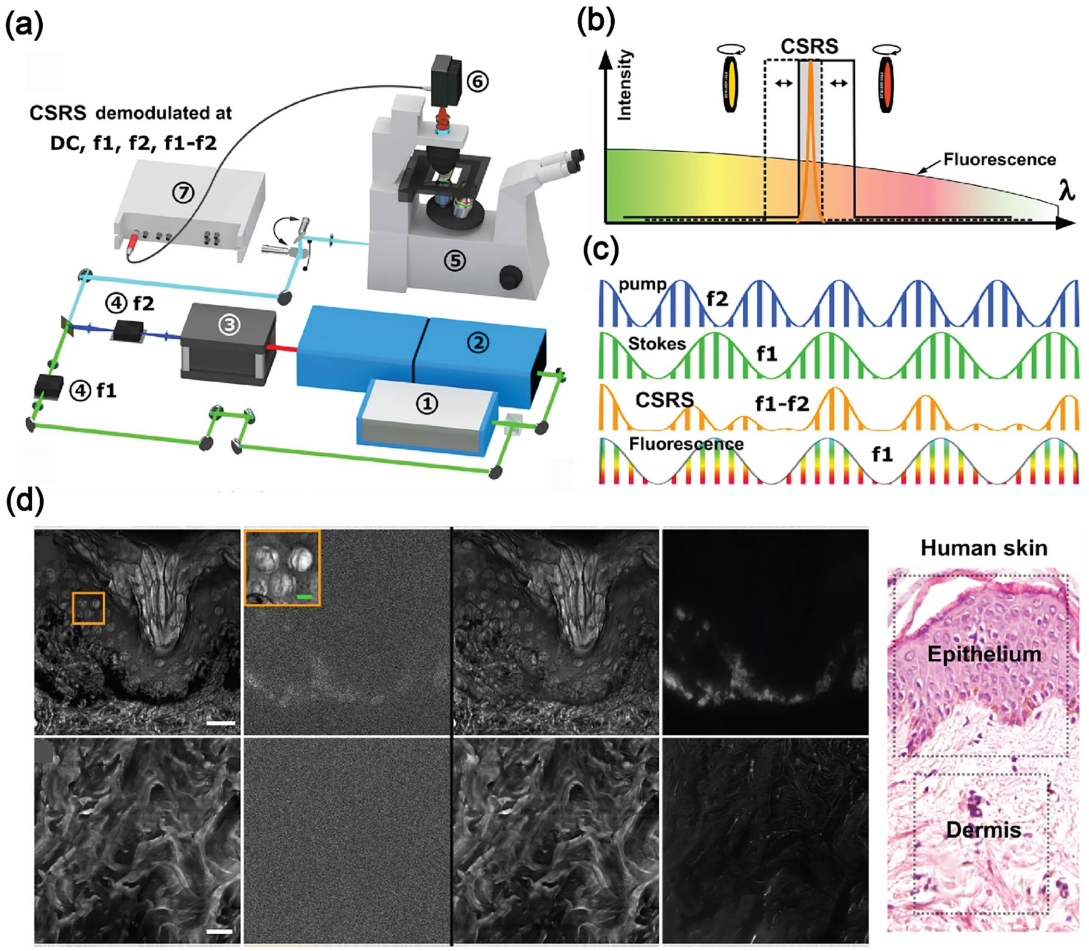

FIG. 5. CSRS microscopy. Reproduced with permission from Heuke and Rigneault, Nat. Commun. **14**, 3337 (2023). Copyright 2023 Springer Nature.[90] (a) Optical layout of CSRS microscope. (b) CSRS signal is separated from fluorescence by means of two angle-tuned narrow bandpass filters. (c) Suppression of fluorescence is achieved by intensity modulating the Stokes and pump beam at different frequencies, f1 and f2, and detecting the CSRS signal at f1–f2. (d) CSRS image of a 20 μm thick human skin section.

sensitivity and stability for biological imaging [Fig. 6(a)].[93] Soon thereafter, Ozeki *et al.* and Nandakumar *et al.* independently advanced the technique, further optimizing its performance. Together, these pioneering developments established the foundation for the rapid evolution and widespread adoption of SRS microscopy in biomedical imaging.[91]

For SRS signal detection, the intensity changes in the pump (ΔI_p, SRL) or Stokes (ΔI_s, SRG) beam are superimposed on the incident light intensity, and the resulting modulation is extremely weak—typically on the order of $\Delta I/I \sim 10^{-5}$.[52] Consequently, modulation–demodulation detection is essential to extract the SRS signal from background noise. A typical SRS microscope consists of a laser-scanning system, two synchronized pulsed-laser beams, an optical modulator, and a demodulator. The excitation beam is intensity-modulated using either an electro-optic modulator (EOM) or an acousto-optic modulator (AOM), with modulation frequencies typically in the megahertz (MHz) range to isolate the weak SRS signal from low-frequency noise. After the transmitted or reflected light is converted into an electrical signal by a high-sensitivity photodetector, the SRS signal is extracted using a demodulator, most commonly a lock-in amplifier [Fig. 6(a)].

a. Multispectral SRS imaging. In SRS microscopy, high-speed multicolor and hyperspectral imaging are essential for capturing the chemical information of biological systems. To expand both spectral acquisition speed and coverage, several strategies have been developed [Fig. 6(b)].

The most straightforward approach to multispectral imaging is to adjust narrowband laser wavelengths. Ozeki *et al.* demonstrated a rapidly tunable laser based on spectral filtering, providing a tuning range of $\sim$300 cm^{-1} and enabling 30 frames/s multicolor imaging.[94] Karpf *et al.* introduced a time-domain encoded multicolor SRS system using a Fourier-domain mode-locked laser, where fiber delay lines mapped different Raman shifts into distinct temporal positions,

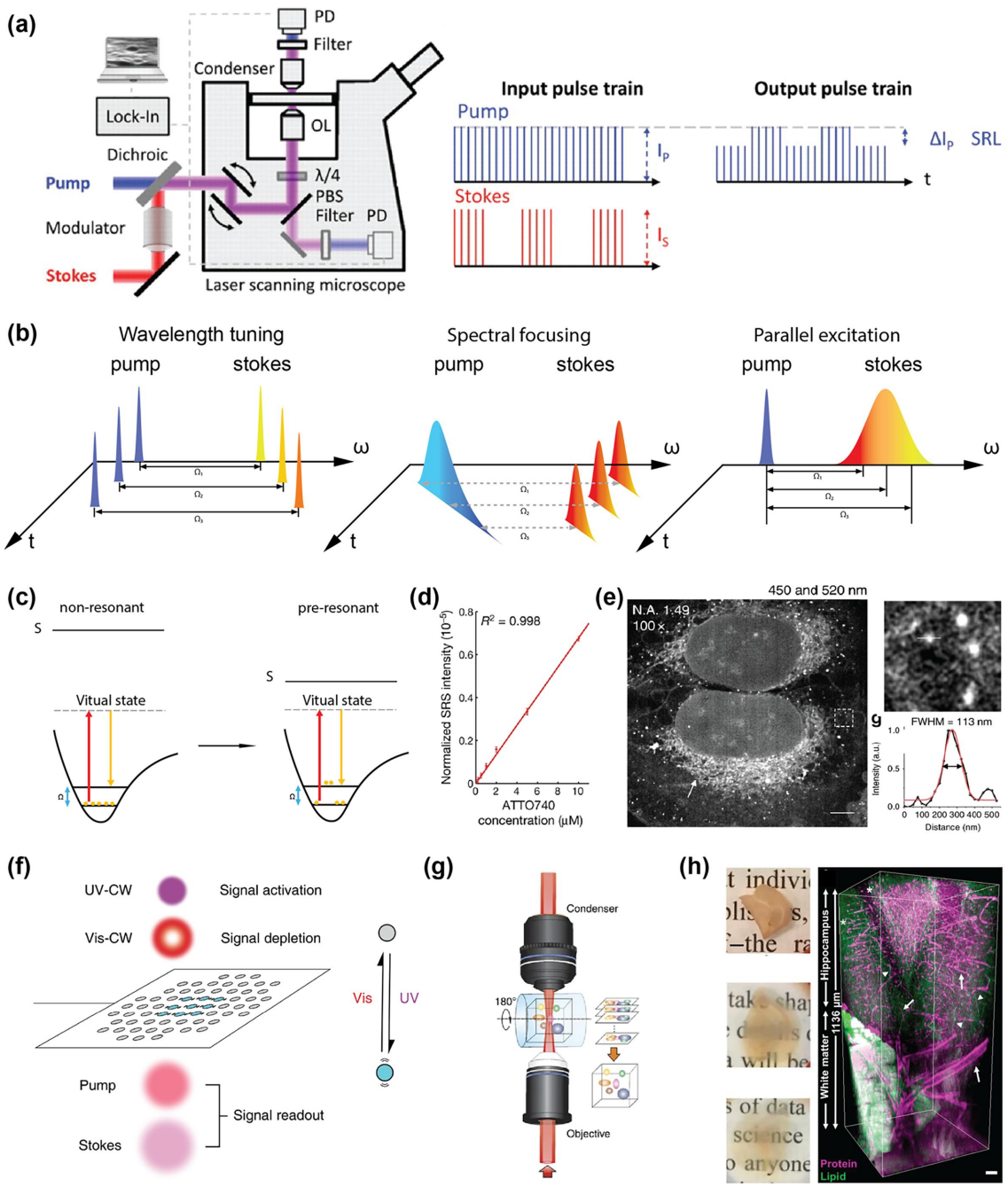

FIG. 6. Developments of SRS microscopy. (a) Typical SRS microscope configuration. Reproduced with permission from Freudiger *et al.*, Science **322**, 1857–1861 (2008). Copyright 2008 American Association for the Advancement of Science.[93] (b) Several strategies to expand both spectral acquisition speed and coverage of SRS. (c) Energy diagram of EPR-SRS. (d) Detection sensitivity of EPR-SRS. Reproduced with permission from Wei *et al.*, Nature **544**, 465–470 (2017). Copyright 2017 Springer Nature.[110] (e) Visible SRS imaging of cultured neurons and U2OS cells. Reproduced with permission from Bi *et al.*, Light: Sci. Appl. **7**, 81 (2018). Copyright 2018 Springer Nature.[115] (f) A donut-shaped beam is introduced to regulate the SRS detection of a photoswitchable Raman probe. Reproduced with permission from Shou *et al.*, Sci. Adv. **9**, eade9118 (2023). Copyright 2023 American Association for the Advancement of Science.[120] (g) Volumetric imaging modalities based on stimulated Raman scattering. Reproduced with permission from Chen *et al.*, Nat. Commun. **8**, 15117 (2017). Copyright 2017 Springer Nature.[125] (h) Volumetric SRS imaging based on a Raman-tailored tissue-clearing method. Reproduced with permission from Wei *et al.*, Proc. Natl. Acad. Sci. U. S. A. **116**, 6608–6617 (2019). Copyright 2019 National Academy of Sciences.[128]

achieving broad spectral coverage with high spectral resolution.[95] Building on the widely tunable all-fiber picosecond laser developed by Brinkmann *et al.*,[96] Ni *et al.* realized broadband hyperspectral imaging spanning 1050–3150 cm^{-1}, covering fingerprint, C–H, and C–D regions.[97]

First proposed by Hellerer *et al.*[62] for CARS imaging and subsequently applied to SRS by Andresen *et al.*,[98] the spectral-focusing technique enhances the spectral resolution of CRS by using chirped broadband pulses. Frequency tuning could be realized by scanning the delay time between the two chirped pulses. The conventional mechanical stage is the simplest but slow means for scanning the time delay, while faster approaches including galvanometer scanners,[99] polygon mirrors,[100] and acousto-optic modulators[101] have been employed to improve the speed for spectral acquisition.

Spectral multiplexing is a powerful alternative for fast hyperspectral imaging. Fu *et al.* proposed a multicolor SRS system combining modulation multiplexing with the fast Fourier transform (FFT) decoding: broadband femtosecond pump light was spectrally divided into narrow spectral subbands by an acousto-optical tunable filter (AOTF) device, each independently modulated at different radio frequencies and recombined with the 1064 nm picosecond Stokes beam. This enabled parallel excitation of multiple Raman channels in a single scan with a spectral resolution of ~33 cm^{-1}.[102] Liao *et al.* achieved microsecond-scale spectroscopic imaging by lock-in free parallel detection of spectrally dispersed SRS signals, obtaining ~200 cm^{-1} fingerprint spectra per pixel within ~32 μs.[103] The same group later introduced a spectrometer-free approach capable of retrieving SRS spectra from highly scattered photons.[104] In the same year, Réhault *et al.* implemented broadband SRS using time-domain Fourier transform detection.[105] He *et al.* split the Stokes light into two beams and introduced a 90° modulation phase shift, enabling simultaneous detection of two Raman frequencies with a single photodetector via the X- and Y-channels of lock-in demodulation.[106,107] Yu *et al.* proposed transient stimulated Raman scattering (T-SRS) microscopy, which encodes vibrational oscillations into SRL signal through the interference of vibrational wave packets generated by two pairs of femtosecond pulse sequences.[108] By Fourier-transforming the time-domain signal, the Raman spectra were retrieved with linewidth-limited resolution and laser-bandwidth-defined spectral coverage. More recently, Guo *et al.* report superbroadband stimulated Raman scattering (SuperB-SRS) that encodes Raman free induction decay into the stimulated Raman loss through few-cycle laser-induced optical interference, permitting universal Raman analysis and imaging that unites high spectral fidelity, natural-linewidth-limited spectral resolution, broad bandwidth, and state-of-the-art sensitivity.[109]

b. Detection sensitivity. The detection sensitivity of conventional SRS microscopy for endogenous molecular vibrations typically lies in the millimolar concentration range.[91] While adequate for imaging systems with high local concentrations such as lipid droplets and protein aggregates, the sensitivity remains insufficient for low-abundance molecular species.

To overcome this limitation, a series of strategies have been developed to enhance the detection sensitivity of SRS microscopy. Wei *et al.* introduced electronic pre-resonance SRS (EPR-SRS), in which the excitation wavelength is tuned near an electronic transition to amplify the Raman response [Fig. 6(c)].[110] This approach achieved 250 nM detection sensitivity of dye ATTO740—a strong Raman probe—with a 1 ms time constant [Fig. 6(d)]. Zong *et al.* demonstrated plasmon-enhanced SRS (PESRS) microscopy, leveraging localized surface plasmon–induced field enhancement.[111] Later, Zhuge *et al.* exploited visible-range electronic pre-resonance to enhance the detection of retinoids down to 34 μM.[112] Most recently, Lin *et al.* reported the ultrasensitive reweighted visible SRS (URV-SRS) integrated with a self-supervised multi-agent denoiser, achieving >7.2 dB noise suppression and a detection limit of ~4000 molecules, representing a 50-fold sensitivity improvement over traditional near-infrared SRS.[113] Oh *et al.* developed electronic resonance stimulated Raman scattering (ER-SRS) microscopy. By combining, in particular, designed Raman-amplified nonfluorescent molecular probes (RANMPs) with an independently tunable double optical parametric oscillator (OPO) system, ER-SRS provides single-molecule sensitivity without fluorescence detection.[114]

c. Spatial resolution. Despite its advantages in chemical contrast and live-cell compatibility, SRS microscopy is still bound by the diffraction limit. This constraint has motivated the development of optical, material-assisted, and computational approaches aimed at achieving sub-diffraction resolution for nanoscale vibrational imaging.

One of the most direct approaches is to reduce the excitation wavelength from the near-infrared to the visible region. Bi *et al.* realized visible SRS microscopy by frequency-doubling femtosecond laser pulses using two beta-barium borate (BBO) crystals, achieving sub-diffraction imaging with a lateral resolution of approximately 130 nm [Fig. 6(e)].[115] Lin *et al.* advanced this concept by introducing Fourier reweighting after NACE denoising (FURNACE), reaching a lateral resolution of 86 nm and an axial resolution of 400 nm in live-cell imaging.[113]

Inspired by concepts from super-resolution fluorescence techniques such as stimulated emission depletion (STED), researchers have adapted analogous saturation mechanisms to improve SRS resolution. Gong and Wang theoretically demonstrated the feasibility of using a donut-shaped Stokes beam to spatially confine the stimulated Raman loss signal at the rim of the focal spot.[116] This concept was experimentally validated by Silva *et al.* who successfully integrated STED with femtosecond SRS to demonstrate super-resolved vibrational imaging.[117] Xiong *et al.* incorporated STED into the stimulated Raman excited fluorescence (SREF), achieving STED-FM-SREF microscopy with more than a twofold resolution improvement across diverse biological specimens.[118]

Beyond saturation-based strategies, the use of photoswitchable vibrational probes combined with nonlinear optical excitation has enabled even finer structural visualization. Ao *et al.* reported super-resolution SRS (SR-SRS) nanoscopy employing ultraviolet excitation and a donut-shaped visible depletion beam to achieve sub-100 nm resolution through reversibly switchable vibrational photochromic probes.[119] Independently, Shou *et al.* achieved comparable performance (~150 nm resolution) using photoswitchable Raman probes [Fig. 6(f)].[120]

Expansion microscopy (ExM) has also been adapted to improve the spatial resolution of SRS. By physically enlarging the sample while preserving molecular composition, ExM effectively bypasses the optical diffraction limit. Qian *et al.* demonstrated hydrogel-based

expansion of biological samples with isotropic dimensional scaling, achieving an effective resolution of 78 nm through optimal retention of endogenous proteins and lipid removal.[121] Shi *et al.* introduced a reversible linear expansion framework enabling up to ∼7-fold enlargement, reaching lateral resolutions down to 41 nm.[122]

4Pi fluorescence microscopy is a well-established approach that enhances both axial resolution and fluorescence sensitivity. Building on this concept, Kim *et al.* combined stimulated Raman scattering (SRS) microscopy with 4Pi interferometry, achieving an approximately sevenfold improvement in axial resolution along with a two- to fourfold increase in sensitivity. Because 4Pi-SRS improves axial resolution through interferometric engineering, it is fundamentally orthogonal to previously reported super-resolution SRS strategies. This orthogonality makes it readily compatible with existing methods and offers a straightforward route toward chemical imaging with substantially higher resolution than was previously achievable.[123]

In parallel, computational advances have significantly contributed to resolution enhancement without modifying the optical setup. Jang *et al.* developed an Adam-optimized pointillism deconvolution (A-PoD) algorithm, enabling sub-59-nm effective resolution in liposome membrane experiments through iterative deconvolution and sparsity-based optimization.[124]

d. Volumetric imaging. Three-dimensional imaging of biological structures plays a vital role in understanding life processes. However, the penetration depth of SRS microscopy is fundamentally limited by optical scattering and aberrations within thick tissues, making volumetric visualization of biological structures and functions a continuing challenge. To overcome these constraints, several strategies have been proposed to enhance volumetric imaging capability. Chen *et al.* developed Bessel-beam-based stimulated Raman projection (SRP) microscopy and tomography, enabling rapid quantification of molecular distributions within 3D samples through two-dimensional lateral scanning combined with rotational sampling [Fig. 6(g)].[125] Wang and Huang further advanced this approach by employing a spatial light modulator to electronically steer the Stokes beam along a needle-shaped Bessel pump beam, thereby achieving volumetric Raman tomography without the need for mechanical z-axis scanning.[126] Nevertheless, Bessel beam-based SRS tomography suffers from system complexity and low beam generation efficiency. An alternative approach is to integrate SRS with optical coherence tomography (OCT). Robles *et al.* combined spectroscopic OCT with SRS, enabling simultaneous spatial and spectral multiplexed imaging.[127] Meanwhile, tissue-clearing methods have also been adopted to enhance penetration depth. Wei *et al.* combined Raman-tailored tissue clearing with SRS microscopy, achieving a >10-fold increase in imaging depth compared with conventional SRS, and enabling deep-tissue, high-resolution, label-free chemical visualization [Fig. 6(h)].[128] Shi *et al.* combined Raman dye imaging and a tissue-clearing (RADIANT) method to achieve multiplexed imaging up to 11 targets in millimeter-thick brain slices, extending imaging depth by one to two orders of magnitude compared with other multiplexing SRS microscopy.[129]

2. Applications

a. Cell biology. As the basic structural and functional units of life, cells exhibit dynamic behaviors that are central to biological processes. SRS microscopy enables label-free and real-time visualization of living cells with subcellular resolution, combining diffraction-limited spatial precision and millisecond temporal response. This technique has successfully been applied to investigate essential cellular processes such as specific metabolites, spectral variations,[130] and even changes in membrane potential.[131] Lu *et al.* achieved label-free imaging of DNA by linear spectral unmixing in the high-wavenumber region and recorded the complete mitotic process through time-lapse SRS imaging, demonstrating the potential of SRS for visualizing genetic material dynamics [Fig. 7(a)].[132] Zhang *et al.* report stimulated Raman-activated cell ejection (S-RACE) that enables high-throughput single-cell sorting by integrating stimulated Raman imaging, *in situ* image decomposition, and laser-induced cell ejection. S-RACE successfully sorted lipid-rich *Rhodotorula glutinis* cells from a cell mixture with a throughput of ∼13 cells/s, and the sorting results were confirmed by downstream quantitative polymerase chain reaction.[133] Sun *et al.* develop *in situ* quantitative imaging of secondary structure in protein condensates. Hyperspectral SRS imaging reveals significant enrichments and disordered to ordered structural changes during phase separation of ALS-related proteins. Time-lapse imaging of the protein aging process directly visualizes heterogeneous β-sheet formation on the condensate surface.[134]

To extend beyond intrinsic vibrational contrast, Raman-active bio-orthogonal probes have been introduced for targeted molecular imaging of specific processes. Deuterated, cyano-, and alkyne-labeled biomolecular analogs have been applied to studies of solid-phase intracellular membrane organization [Fig. 7(b)],[135] the environment–micro-organism–host metabolic axis,[136] lipid peroxidation during ferroptosis,[137] glucose metabolism,[138] and deuterium tracing of water metabolism.[138–140]

In addition to these probes, Wei introduced MARS supermultiplexed probes that achieve 24-color imaging, revealing cell-type-dependent heterogeneities in DNA and protein metabolism under physiological and pathological conditions.[110] The same group subsequently introduced &Carbow probes,' providing 20 discrete Raman frequencies, and combined five organelle-targeted Carbow probes with five fluorescent reporters to achieve ten-color optical imaging of subcellular structures in living cells [Fig. 7(c)].[141]

b. Stimulated Raman histology. In histopathology, real-time imaging of fresh surgical specimens is critical for intraoperative diagnosis. Stimulated Raman histology (SRH) provides label-free molecular contrast comparable to conventional hematoxylin and eosin (H&E) staining. In 2013, Ji *et al.* demonstrated the first *in vivo* delineation of brain tumor margins in a glioblastoma (GBM) xenograft mouse model using lipid-and-protein (L&P) imaging in the epi-detection mode [Fig. 7(d)].[142] Since then, SRS microscopy has been applied to tumor diagnostics across multiple cancer types, including brain,[142–145] breast,[146–149] gastric,[150] and prostate cancers,[151] enabling rapid assessment of tumor infiltration and intratumoral heterogeneity.[152]

Integration of artificial intelligence with SRH has further improved diagnostic efficiency. Deep-learning frameworks including cross-modality transformation,[150,153,154] semantic segmentation,[148,151,155–157] and virtual staining[158–160] have achieved highly accurate digital diagnoses. Hollon *et al.* combined SRH with deep convolutional neural networks (CNNs) to perform intraoperative

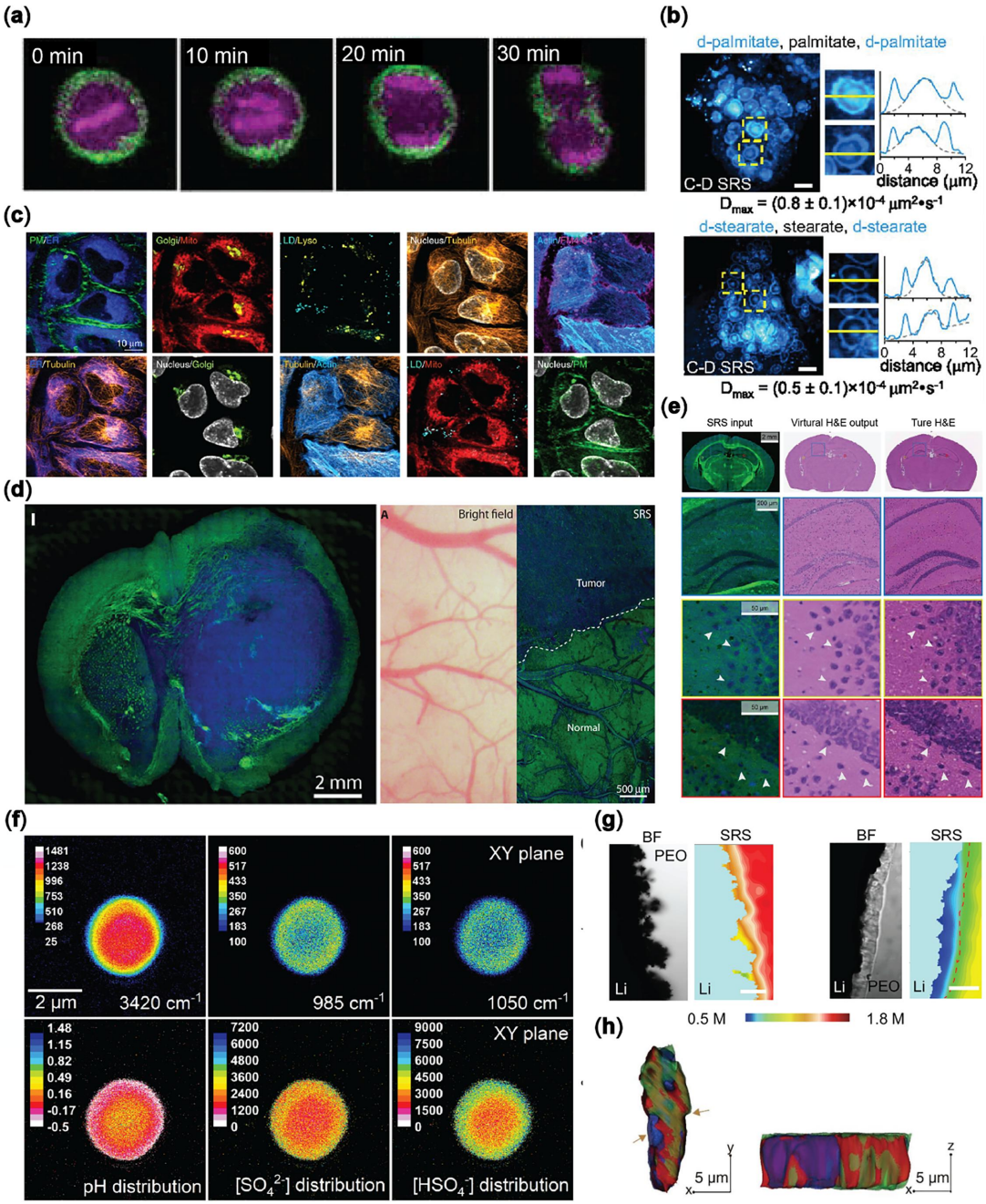

FIG. 7. Applications of SRS microscopy. (a) Label-free imaging of DNA in HeLa cells using SRS. Reproduced with permission from Lu *et al.*, Proc. Natl. Acad. Sci. U. S. A. **112**, 11624–11629 (2015). Copyright 2015 National Academy of Sciences.[132] (b) SRS imaging of deuterated fatty acids. Reproduced with permission from Shen *et al.*, Proc. Natl. Acad. Sci. U. S. A. **114**, 13394–13399 (2017). Copyright 2017 National Academy of Sciences.[135] (c) Ten-color optical imaging of live HeLa cells with targeted Carbow probes. Reproduced with permission from Hu *et al.*, Nat. Methods **15**, 194–200 (2018). Copyright 2018 Springer Nature.[141] (d) Brain tumor margin images in human GBM xenograft mouse model by SRS microscope. Reproduced with permission from Ji *et al.*, Sci. Transl. Med. **5**, 201ra119 (2013). Copyright 2013 American Association for the Advancement of Science.[142] (e) Contrasting images of SRS, converted to virtual H&E and HE images. Reproduced with permission from Liu *et al.*, Sci. Adv. **10**, eadn3426 (2024). Copyright 2024 American Association for the Advancement of Science.[159] (f) SRS images of microdroplets at the Raman shifts of 3420 cm^{-1} (H_2O), 985 cm^{-1} (SO_4^{2-}), and 1050 cm^{-1} (HSO_4^-) pH distribution. Reproduced with permission from Gong *et al.*, Proc. Natl. Acad. Sci. U. S. A. **120**, e2219588120 (2023). Copyright 2023 National Academy of Sciences.[164] (g) The bright-field and corresponding SRS images between the boundary between the lithium electrode and the PEO electrolyte. Reproduced with permission from Cheng *et al.*, Joule **6**, 2372–2389 (2022). Copyright 2022 Elsevier B.V.[166] (h) the 3D reconstructed structure of individual atmospheric aerosols with nitrate (green), sulfate (red), and oxalate (blue). Reproduced with permission from Ao *et al.*, Small Methods **4**, 1900600 (2020). Copyright 2020 Wiley-VCH.[169]

brain tumor diagnosis within 150 s, reaching an overall accuracy of 94.6%.[155] Liu *et al.* applied a U-Net-based model to convert femtosecond SRS images into dual-color picosecond contrasts, achieving automated tissue differentiation in gastroscopic biopsies.[150] In 2024, the same group developed a hybrid supervised CycleGAN framework to generate virtual H&E stains from fresh brain tissue SRS images, allowing precise identification of histologic subtypes of brain tumors [Fig. 7(e)].[159] Kondepudi *et al.* presented FastGlioma, an artificial intelligence diagnostic system for rapid intraoperative clinic trials on glioma detection. They trained the model using 4×10^6 SRH images collected from 11 000 surgical specimens, enabling detection and quantification of tumor infiltration in fresh, unprocessed, unlabeled surgical tissue within less than 10 s.[161] By providing quantification of tumor infiltration at the resection margins, the system allows surgeons to achieve maximal safe resection while sparing healthy brain tissue. Ma *et al.* presented DeepLuAd—an artificial intelligence diagnostic platform for the precise grading and pixel-level segmentation of lung adenocarcinoma. By providing objective area calculations for high-grade patterns, the system allows clinicians to achieve accurate risk stratification and optimized surgical margin assessment while managing the complex heterogeneity of lung tissues.[162]

c. Physical chemistry. Beyond its biomedical applications, SRS microscopy has also become a versatile tool in physical chemistry research. Chen *et al.* applied *in situ* SRS imaging to investigate the phase transition between ice Ih and ice XI by tracking changes in the OH stretching vibrations.[163] Gong *et al.* visualized the three-dimensional pH distributions within microdroplets of varying sizes [Fig. 7(f)],[164] while Xiong *et al.* quantified interfacial electric fields up to 10^7 V cm^{-1} at water–oil interfaces using nitrile-based vibrational Stark probes.[165] Cheng *et al.* employed operando SRS microscopy to monitor ion depletion and dendrite growth in lithium batteries, as well as phase transitions in polymer electrolytes [Fig. 7(g)].[166,167] In addition, Li *et al.* utilized a collinear multi-beam SRS setup to observe propagating polymerization waves driven by reaction kinetics and sustained ultraviolet initiation.[168] These studies demonstrate the capability of SRS microscopy to directly visualize molecular structure and dynamics in various materials.

d. Environmental science. SRS microscopy has recently shown great potential in environmental science for chemical imaging and pollutant analysis. Ao *et al.* first demonstrated nondestructive three-dimensional chemical imaging of single aerosol particles, revealing detailed internal distributions and mixing states of nitrates and sulfates in atmospheric aerosols [Fig. 7(h)].[169] In 2023, the same group applied SRS microscopy for rapid detection and 3D visualization of micro- and nanoplastics, successfully identifying particles as small as 100 nm and distinguishing polymer types through combined high- and low-wavenumber spectral analysis.[170] Qian *et al.* integrated SRS with a spectral matching algorithm to detect nanoplastics in bottled water, identifying multiple polymer types with concentrations of approximately 2.4×10^5 particles per liter, of which nearly 90% were nanosized. This is orders of magnitude more than the microplastic abundance reported previously in bottled water.[171] In the same year, Wang *et al.* utilized SRS spectral signatures to differentiate and quantify microplastics accumulated within protozoa, enabling visualization of both single and mixed microplastic uptake.[172] These studies demonstrate SRS microscopy as an emerging platform for multidisciplinary research through label-free chemical imaging.

E. Stimulated-Raman-excited imaging modalities

1. Stimulated Raman photothermal (SRP) microscopy

SRP microscopy leverages the stimulated-Raman-excited photothermal effect to achieve higher sensitivity.[173] As described above, during SRS process the annihilation of pump photons and the simultaneous generation of Stokes photons result in the energy transfer from electromagnetic field to molecular vibrational states. The excited molecules quickly relax to the ground state through nonradiative decay, releasing the vibrational energy as local heat. Thus, while the optical energy by itself appears non-conserved, the combined system of light and matter remains fully energy-conserving, with the excess energy accounted for by molecular vibrations and subsequent thermal dissipation.

Under typical SRP conditions, the repeated excitation at MHz repetition rates causes heat to accumulate within the excitation volume on a microsecond timescale, resulting in localized thermal buildup [Fig. 8(a)]. Zhu *et al.* demonstrated that SRP could induce a temperature rise of several kelvin.[173] The local temperature rise will further induce a negative refractive index change, resulting in a divergent thermal lens that can be sensitively detected with a tightly focused probe beam. To describe this mechanism, a ball-lens model was built to provide a simplified yet intuitive framework for how refractive index changes alter beam propagation and generate contrast in SRP imaging. Under paraxial approximation, the detected SRP signal scales with three main factors: (1) the number of SRS events, (2) the vibrational energy per transition, and (3) the efficiency with which temperature changes are converted into refractive index modulation,

$$I_{SRP} \propto N\sigma_{SRS}\phi_{pump}\phi_{Stokes}\tau_{ex} \cdot \hbar\omega_{SRS} \cdot \frac{1}{V_{SRS}} \cdot \frac{1}{C_P n_0} \cdot \frac{dn}{dT}. \quad (13)$$

Here, SRS is conceptualized as a two-photon vibrational excitation process.[174] N is the number of molecules within the excitation volume, σ_{SRS} is the cross section of SRS, ϕ_{pump} and ϕ_{Stokes} are the photon fluxes of the pump and Stokes beams, and τ_{ex} is the pulse duration. Together, the first term $N\sigma_{SRS}\phi_{pump}\phi_{Stokes}\tau_{ex}$ represents the number of SRS events. The second term, $\hbar\omega_{SRS}$, corresponds to the energy of vibrational transition. Multiplexing the first and second term yields the entire energy deposited into the sample. The third term characterized the thermal and optical properties of the local environment, where V_{SRS} is the SRS excitation volume, C_P is the heat capacity of the surrounding environment, n_0 is the refractive index, and dn/dT is the thermo-optic coefficient. This factor determines how efficiently deposited heat is converted into a refractive index change. Unlike conventional SRS detection, which directly monitors small changes in optical intensity, this environmental term provides additional opportunities to enhance SRP signal by tailoring the medium's thermal and optical characteristics.

Compared with SRS, SRP provides several advantages. First, the thermal lensing effect can be amplified in thermal enhancement media, such as glycerol or urea, yielding a much higher modulation depth and superior sensitivity. Second, SRP detection is insensitive to intensity fluctuations in the pump and Stokes beams, allowing the use of noisy fiber lasers or optical parametric amplifiers (OPAs) that are

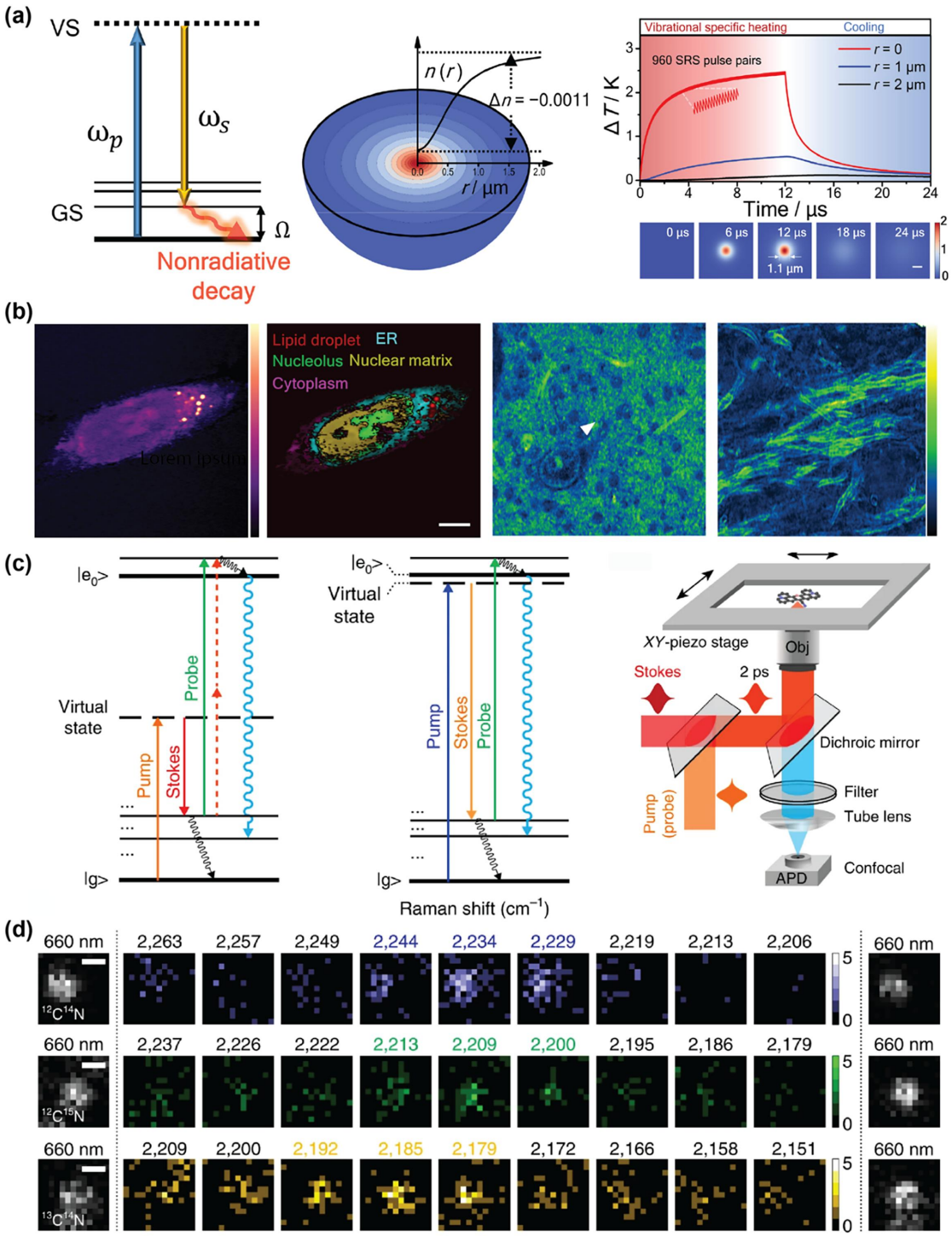

FIG. 8. Stimulated Raman-excited imaging modalities. (a) Theoretical simulation and experimental observation of the SRP effect. Reproduced with permission from Zhu *et al.*, Sci. Adv. **9**, eadi2181 (2023). Copyright 2023 American Association for the Advancement of Science.[173] (b) SRP imaging of biological samples in an aqueous environment. Reproduced with permission from Zhu *et al.*, Sci. Adv. **9**, eadi2181 (2023). Copyright 2023 American Association for the Advancement of Science.[173] (c) Energy diagrams of SREF and experimental setup. Reproduced with permission from Xiong *et al.*, Nat. Photonics **13**, 412–417 (2019). Copyright 2019 Springer Nature.[176] (d) Single-molecule SREF images of Rh800 isotopologs. Reproduced with permission from Xiong *et al.*, Nat. Photonics **13**, 412–417 (2019). Copyright 2019 Springer Nature.[176]

unsuitable for conventional SRS.[175] Third, since SRP detects thermally induced refractive index changes rather than directly measuring scattered photons, it can employ long working-distance objectives, leaving ample space for experiments involving flow cytometry chips, multiwell plates, or live tissue imaging. One limitation is the potential background from non-vibrational absorption, which can be reduced by optimizing pulse conditions. Overall, SRP combines high sensitivity and experimental flexibility, offering a versatile platform for bond-selective imaging in both biological and material studies [Fig. 8(b)].

2. Stimulated Raman excited fluorescence (SREF) microscopy

SREF couples the vibrational excitation generated by SRS to an electronic fluorescence pathway, merging the chemical specificity of Raman transitions with the single-molecule sensitivity of fluorescence detection. Two synchronized pulsed beams—the pump and Stokes—coherently populate the intermediate vibrational state from the molecular ground state $|g\rangle$ through stimulated Raman excitation. A third probe beam, often the pump beam itself, promotes the vibrational population to an electronic excited state [Fig. 8(c)]. Unlike conventional fluorescence spectroscopy, SREF is a Raman-mediated three-photon process. By tuning the Raman detuning ($\omega_p - \omega_s$), the resulting fluorescence excitation spectrum directly encodes the vibrational resonance, effectively translating Raman information into a fluorescent readout. Under pre-resonant conditions—where the pump wavelength is slightly detuned below the electronic absorption maximum—the Raman cross section can increase by several orders of magnitude while minimizing anti-Stokes fluorescence background [Fig. 8(c)].[176]

Experimentally, temporally and spatially overlapped pump and Stokes pulses are focused into the sample, and the resultant fluorescence is detected in the backward direction with a single-photon avalanche diode. Using near-infrared dyes such as Rhodamine 800 and ATTO 740, SREF spectra exhibit narrow Raman-like peaks embedded within the fluorescence excitation profile, consistent with the corresponding SRS vibrational frequencies. Owing to fluorescence detection, SREF achieves ~100-fold higher sensitivity than SRS, enabling detection limits below 10 nM and allowing single-molecule Raman spectroscopy and imaging without plasmonic enhancement.

Beyond its sensitivity, SREF provides powerful multiplexing capability. Because isotopically substituted dyes exhibit identical electronic spectra but distinct vibrational frequencies, SREF can resolve multiple labels within a single fluorescence channel, thereby breaking the long-standing "color barrier" of fluorescence microscopy. Using isotopically edited Rh800 derivatives, SREF has demonstrated four-color vibrational imaging of living *E. coli* cells and single-molecule discrimination in polymer matrices [Fig. 8(d)].[176]

In summary, SREF represents a Raman-mediated multiphoton fluorescence process that unites vibrational specificity with single-molecule sensitivity. Together, SRP and SREF exemplify a new generation of stimulated Raman–excited imaging modalities that convert molecular vibrations into thermally or radiatively amplified optical signals, expanding coherent Raman microscopy toward ultrahigh sensitivity, multiplexed chemical imaging, and single-molecule detection.

V. STIMULATED BRILLOUIN SCATTERING (SBS) MICROSCOPY

A. Principle of SBS microscopy

Unlike Raman scattering, which probes local chemical bonds or optical phonons in the higher frequency range (>1 THz), Brillouin scattering detects acoustic phonons in the lower frequency range (MHz–GHz).[177] Similar to spontaneous Raman scattering, spontaneous Brillouin scattering is excited by a single pump beam, relies on thermally excited acoustic waves, and is a linear optical process. Analogous to SRS, SBS is also a third-order nonlinear optical process that requires simultaneous illumination with pump and Stokes beams.[178] The pump (frequency ω_1) and Stokes (frequency ω_2) beams counter-propagate and are focused into a common focal point within the sample. The slight frequency difference, $\Omega_B = \omega_1 - \omega_2$, between the two beams generates a traveling intensity interference pattern [Fig. 9(a)]. Through the electrostrictive effect, this interference pattern creates a periodic pressure field, which coherently excites an acoustic wave with frequency Ω_B. This acoustic wave induces a traveling refractive index grating. The pump beam undergoes Bragg diffraction from this grating, producing Doppler-shifted light at frequency $\omega_2 = \omega_1 - \Omega_B$. Energy and momentum conservation dictate that the diffracted light and the incident Stokes beam share the same frequency, phase, and propagation direction. Their coherent superposition leads to amplification of the Stokes beam, thereby enhancing the Brillouin scattering signal in a process analogous to stimulated emission. Stimulated Brillouin gain (SBG) is defined as the amplification of the Stokes beam intensity, whereas stimulated Brillouin loss (SBL) corresponds to the attenuation of the pump beam intensity [Fig. 9(b)].

The scattering efficiency of spontaneous Brillouin scattering is extremely low (typically on the order of 10^{-9} for the power ratio of scattered to incident light),[179] resulting in low sensitivity and slow imaging speed in microscopy techniques based on it.[180,181] In contrast, SBS can enhance the signal strength by up to six orders of magnitude, leading to significant improvements in both the sensitivity and imaging speed of SBS microscopy. Although recent technical advances have substantially improved the imaging speed of spontaneous Brillouin microscopy,[182–184] its spectral resolution remains a persistent limitation. In SBS microscopy, the pump frequency is fixed, and the Stokes frequency is scanned to acquire the Brillouin spectrum. Its spectral precision is limited solely by the laser linewidth and is independent of dispersive elements, such as Fabry–Pérot interferometers and virtually imaged phased array (VIPA), whose instrument linewidth broadens measured Brillouin spectra in spontaneous Brillouin microscopy. The Brillouin spectral profile of a pure substance exhibits a Lorentzian line shape, as illustrated by that of high-purity water in Fig. 9(c).[185] The peak position and full width at half-maximum (FWHM) of the spectrum correspond to the Brillouin shift Ω_B and the Brillouin linewidth Γ_B, respectively. These two parameters are related to the material's complex longitudinal modulus according to the following relationship:[186]

$$M = M' + iM'' = \frac{\pi^2 c^2 \rho}{{\omega_1}^2 n^2}\left({\Omega_B}^2 + i\Omega_B\Gamma_B\right), \tag{14}$$

where M′ and M″ are the storage and loss moduli, accounting for the elasticity and viscosity of the material, respectively; ρ, n, and c are the mass density, refractive index, and speed of light in a vacuum,

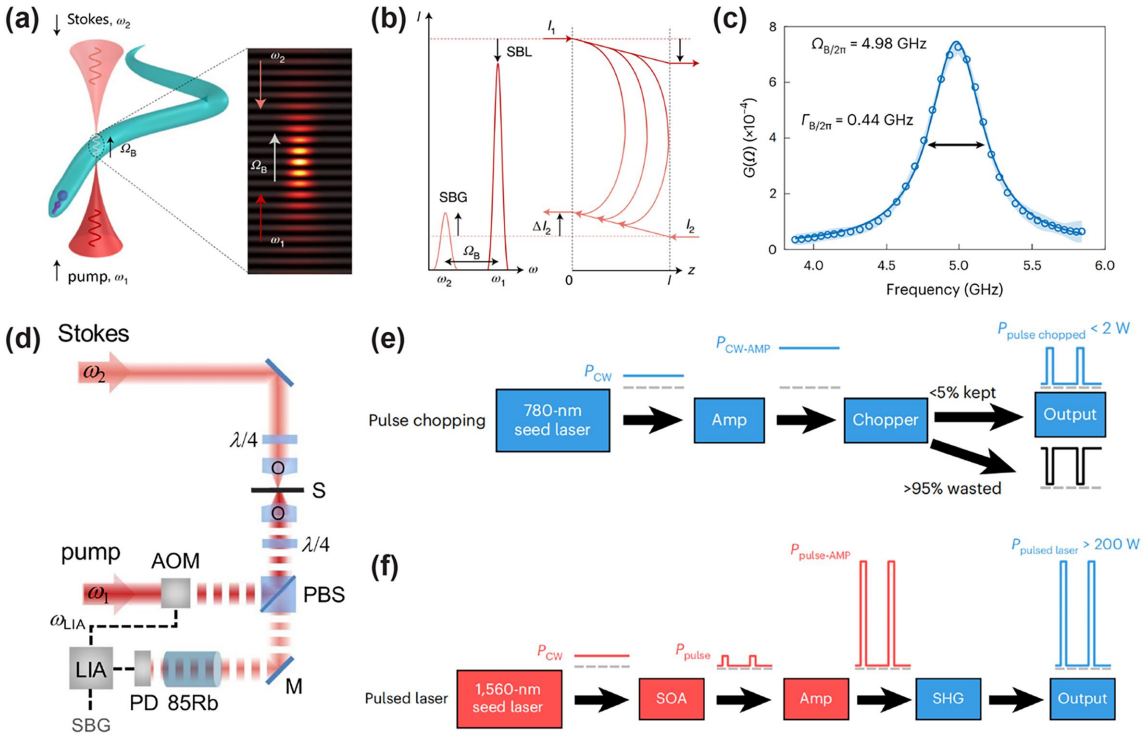

FIG. 9. Principles and methods of SBS microscopy. (a) Acousto-optic interaction between counter-propagating pump (ω_1) and Stokes (ω_2) light with a longitudinal acoustic phonon (Ω_B) via optical interference (stripe pattern) and acoustic resonance (gray wavefronts). Reproduced with permission from Remer *et al.*, Nat. Methods **17**, 913–916 (2020). Copyright 2020 Springer Nature.[199] (b) Intensity transfer between the pump (I_1) and the Stokes (I_2) light by virtue of SBS, with an intensity increase in the Stokes beam (ΔI_2, SBG) and an intensity decrease in the pump beam (SBL). Reproduced with permission from Remer *et al.*, Nat. Methods **17**, 913–916 (2020). Copyright 2020 Springer Nature.[199] (c) SBS spectra of water. Reproduced with permission from Qi *et al.*, Nat. Photonics **19**, 879 (2025). Copyright 2025 Springer Nature.[185] (d) Schematic of SBS microscopy. Reproduced with permission from Bilenca *et al.*, J. Phys. Photonics **6**, 032001 (2024). Copyright 2024 IOP Publishing.[177] (e) Schematic of the quasi-continuous-wave approach. A CW 780-nm seed laser is amplified and then chopped by an optical modulator. Reproduced with permission from Qi *et al.*, Nat. Photonics **19**, 879 (2025). Copyright 2025 Springer Nature.[185] (f) Schematic of the pulse generation approach. A CW 1560-nm seed laser is passed through a pulse generator, followed by pulsed amplification and SHG to produce high-peak-power pulses at 780 nm. Reproduced with permission from Qi *et al.*, Nat. Photonics **19**, 879 (2025). Copyright 2025 Springer Nature.[185]

respectively. For samples with known density and refractive index, the mechanical properties can be directly derived from the Brillouin spectrum.

B. Instrumental evolution

SBG spectroscopy[187–191] and impulsive SBS (iSBS) spectroscopy[192] were first established in the 1980s and 1990s, providing high-resolution measurement of Brillouin spectra in diverse materials.[193–195] By combining SBG/iSBS spectroscopy and microscopy, (i) SBS microscopy[196–198] has been devised, achieving imaging of non-biological samples with high spectral resolution but at limited spatiotemporal resolution. In 2020, Remer *et al.*[199] developed the first continuous-wave SBS (CW-SBS) microscope designed for life sciences applications, enabling *in vivo* imaging of longitudinal elastic and viscous moduli. In 2023, Yang *et al.*[200] and Chow and Yun[201] independently reported quasi-continuous-wave SBS (QCW-SBS) microscopes. In these systems, continuous-wave lasers are chopped using acousto-optic modulators (AOMs) and electro-optic modulators (EOMs) to generate quasi-CW beams, an approach that significantly reduces phototoxicity while maintaining imaging quality. In 2024, Shaashoua *et al.*[202] introduced the concept of Brillouin gain microscopy (BGM), which enables single-frame Brillouin gain imaging without the need for full spectral scanning. In 2025, Qi *et al.*[185] developed a pulsed-laser SBS (PL-SBS) microscope utilizing custom high-peak-power nanosecond pulsed lasers. This approach increased imaging speed by two orders of magnitude and facilitated real-time Brillouin imaging of living specimens.

1. Continuous-wave SBS (CW-SBS) microscopy

The earliest SBS microscope employed CW lasers, typically at a wavelength of 780 nm, which featured narrow linewidths and a tunable range exceeding 30 GHz, as illustrated in Fig. 9(d).[177] The pump beam frequency is fixed, but its amplitude is modulated by an AOM, while the Stokes beam frequency is scanned near the acoustic resonance frequency of the sample. The Stokes beam detected by the photodetector contains a CW component and an SBS-induced component modulated at the frequency of the AOM. By employing a lock-in amplifier that is referenced to the modulation frequency of the

pump beam, the SBG signal is extracted, and the Brillouin spectrum is recorded by scanning the frequency of the Stokes beam.

Subsequent improvements to the initial CW-SBS microscope design enabled its application in *in vivo* imaging.[199] These enhancements included: (1) The use of a high-NA objective lens to reduce the focal spot size and increase energy density, significantly enhancing spatial resolution and signal generation efficiency. (2) Achieving shot-noise-limited sensitivity by employing a custom transimpedance photodetector. (3) Utilizing a heated Rubidium-85 atomic vapor filter to efficiently eliminate the stray pump beam from the sample. (4) Increasing the modulation/demodulation frequency from kHz to MHz to avoid low-frequency laser and environmental noise, thereby boosting the signal-to-noise ratio (SNR). Although the single-pixel spectral acquisition time in CW-SBS microscopes has been reduced to 20 ms, the high average power at the sample (168–265 mW)[199,203] induces substantial phototoxicity, which remains a major limitation for broader applicability.

2. Quasi-continuous-wave SBS (QCW-SBS) microscopy

To reduce phototoxicity, QCW-SBS microscopy utilizes CW lasers that are chopped by AOMs to produce a quasi-pulsed excitation scheme [Fig. 9(e)].[200,201] When the pump and Stokes quasi-pulses are spatiotemporally overlapped in the sample with a duty cycle of κ, the average powers of the pump and Stokes beams, I_1 and I_2, are related to their peak powers, I_1/κ and I_2/κ. The SBG signal generated within a single cycle is given by

$$\langle \Delta I_2 \rangle \propto \frac{\int_0^T I_1 I_2 \mathrm{d}t}{T} = \frac{\int_0^{\kappa T} I_1 I_2 \mathrm{d}t}{\kappa^2 T} = \frac{I_1 I_2}{\kappa}. \tag{15}$$

The signal intensity is proportional to the average power of the pulses but inversely proportional to the duty cycle κ. Thus, quasi-continuous-wave excitation enhances the peak power, which reduces the average power required to generate an equivalent signal intensity, thereby mitigating phototoxicity. For a fixed single-pixel acquisition time of 20 ms, QCW-SBS microscopy reduces the total illumination power from 168–265 to 27–55 mW, thereby facilitating *in vivo* observation of diverse biological specimens. Another critical advancement in QCW-SBS microscopy is the integration of a balanced detector, which effectively suppresses relative intensity noise (RIN). This noise suppression ensures a shot noise-limited performance comparable to that of CW-SBS microscopy. However, the acquisition of a 500×500 pixel spectral image using QCW-SBS still requires over 1.3 h. Owing to the limited peak power (typically 1–2 W) achievable with CW lasers, the imaging speed of QCW-SBS cannot be substantially increased by further elevating the peak power and reducing the duty cycle.

3. Brillouin gain microscopy (BGM)

Conventional SBS microscopy requires scanning the entire Brillouin spectrum (typically spanning 2–4 GHz) to determine the Brillouin shift and linewidth. To address this limitation, Shaashoua *et al.*[202] introduced the concept of BGM. This technique acquires images by measuring the Brillouin gain at a single, predefined frequency, thereby eliminating the need for time-consuming spectral scanning. Consequently, BGM reduces the single-pixel acquisition time from 20 ms to 100 μs and the excitation energy to 23 μJ. These improvements make the technique particularly suitable for long-term *in vivo* imaging. Additionally, BGM incorporates an optimized optical filtering system featuring a temperature-controlled solid etalon. This system provides an integrated optical noise suppression of 20 dB and an overall optical density of 6. This effectively eliminates baseline drift induced by reflection of the pump beam, which is critical for ensuring the reliability of single-frequency detection.

4. Pulsed-laser SBS (PL-SBS) microscopy

A higher-peak-power pulse with reduced pulse width and duty cycle can enhance the imaging speed without increasing the average power. Notably, Brillouin scattering requires excitation with nanosecond pulses, unlike the picosecond or femtosecond pulses typically employed in other nonlinear microscopy techniques. To this end, Qi *et al.*[185] developed a custom high-peak-power nanosecond pulsed fiber laser for SBS, thereby implementing a genuine pulsed-laser SBS microscope. The quasi-CW scheme follows an "amplify first, then chop" approach [Fig. 9(e)].[200,201] This method is inherently inefficient, as most of the pulse energy is wasted, resulting in a limited peak power of only 1–2 W. In contrast, the pulsed scheme is based on a "chop first, then amplify" strategy [Fig. 9(f)].[185] Here, nanosecond seed pulses are first generated at 1560 nm, then undergo a two-stage fiber amplification and second harmonic generation (SHG) to produce high-peak-power pulses at 780 nm. This method efficiently concentrates the pump energy within the pulse duration, increasing the peak power by two orders of magnitude to 267 W. To mitigate the intensity noise introduced by the fiber amplification process, an automatically balanced detection system was implemented. This system uses a proportional–integral–derivative (PID) regulator to dynamically adjust an electronic variable optical attenuator (EVOA) in the reference path, maintaining consistent optical power between the signal and reference arms. This achieves a noise suppression of up to 31.3 dB, a significant improvement over traditional balanced detection. The PL-SBS microscope reduces the single-pixel spectral acquisition time from 20 ms to 200 μs. Consequently, a 500×500 pixel spectral image can be acquired in just a few minutes. When operating in Brillouin gain microscopy (BGM) mode at a single frequency, the PL-SBS system achieves a pixel dwell time of 5 μs. These capabilities collectively position PL-SBS microscopy as a powerful tool for a wide range of applications in biomechanics.

C. Applications of SBS microscopy

In 2016, the first SBS microscope successfully achieved 2D imaging, demonstrating the technique's capability for mechanical imaging of transparent media such as water. Since the introduction of the first life-sciences-dedicated SBS microscope in 2020, SBS-based bioimaging has been validated in diverse biological systems. CW-SBS microscopy obtained images of live *C. elegans* nematodes at both organ and subcellular levels [Figs. 10(a) and 10(b)],[199] and was also employed to map the Brillouin shift, linewidth, and gain contrast in individual cells, such as NIH/3T3 fibroblasts.[204]

Owing to its low average power, QCW-SBS microscopy facilitates imaging of light-sensitive specimens. It has been applied for high-resolution 3D Brillouin imaging of various cell types, including

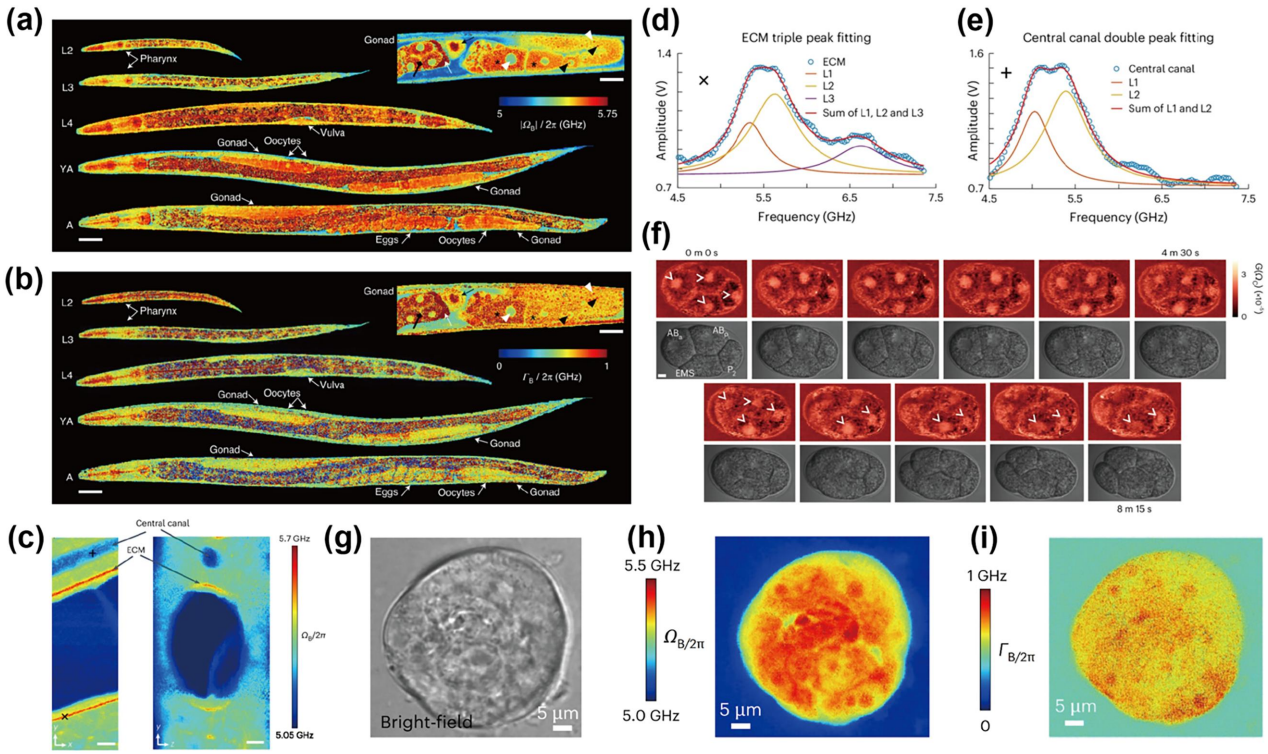

FIG. 10. Applications of SBS microscopy. SBS images of Ω_B (a) and Γ_B (b) of live nematodes at three larval stages (L2, L3, and L4) and two adult stages, young adult (YA) and adult (A). The insets display SBS images at subcellular resolution of Ω_B (a) and Γ_B (b) of the posterior gonad arm in a live adult nematode. Reproduced with permission from Remer *et al.*, Nat. Methods **17**, 913–916 (2020). Copyright 2020 Springer Nature.[199] (c) Brillouin shift image of the x–y (left) and y–z (right) planes of the notochord region of a zebrafish larva at 3 dpf stage. Reproduced with permission from Yang *et al.*, Nat. Methods **20**, 1971–1979 (2023). Copyright 2023 Springer Nature.[200] Brillouin spectrum in the high-shift region (d), indicative of ECM, marked by a cross in (c), and in the spinal cord region (e), marked by a plus sign in (c). Reproduced with permission from Yang *et al.*, Nat. Methods **20**, 1971 (2023). Copyright 2023 Springer Nature.[200] (f) Time-lapse BGM and bright-field imaging of early wild-type *C. elegans* embryonic development. Reproduced with permission from Shaashoua *et al.*, Nat. Photonics **18**, 836–841 (2024). Copyright 2024 Springer Nature.[202] Bright-field (g), Brillouin shift (h), and Brillouin linewidth (i) imaging of a patient-derived lung cancer tumor organoid. Reproduced with permission from Qi *et al.*, Nat. Photonics **19**, 879 (2025). Copyright 2025 Springer Nature.[185]

NIH/3T3 fibroblasts, primary human brain microvascular endothelial cells (HBMECs), mouse embryonic stem (mES) cells,[200] and HeLa cells.[201] Furthermore, this technique has enabled monitoring of mechanical properties during early development of mouse embryos, mouse mammary gland organoids, and *C. elegans* embryos (full-spectrum scans at 13-min intervals for over 3 h) while sample viability is maintained. The high mechanical specificity of QCW-SBS microscopy also allows differentiation of multiple mechanical components within the zebrafish larval notochord [Figs. 10(c)–10(e)].[200]

BGM captures Brillouin gain images at a specific frequency, providing high mechanical contrast and significantly improved imaging speed for rapid biomechanical dynamics. This method has achieved *in vivo* imaging in *C. elegans* nematodes, revealing mechanical contrast between the stiffer pharynx and softer surrounding pharyngeal tissues. It has also resolved subtle mechanical differences between the nucleoplasm and nucleoli in NIH/3T3 fibroblasts and enabled time-lapse imaging of early *C. elegans* embryonic development, tracking nuclear mechanical changes during cell division with single-frame scans at 45-s intervals [Fig. 10(f)].[202]

PL-SBS microscopy further increases imaging speed by two orders of magnitude, demonstrating robust performance in complex biological specimens. It clearly resolved subcellular structures in HeLa cells, NIH/3T3 fibroblasts, human leukemia (MOLM-13) cells, human osteosarcoma (U2OS) cells, and zebrafish ovarian follicles. Remarkably, it has achieved high-quality imaging of human lung cancer tumor organoids for the first time [Figs. 10(g)–10(i)]. Additionally, PL-SBS can distinguish mechanical components in the zebrafish notochord and has been used for time-lapse imaging of *C. elegans* embryo development *in vivo* with full-spectrum scans at 90-s intervals.[185]

VI. DISCUSSION

Coherent nonlinear vibrational microscopy fundamentally enables label-free chemical imaging by directly probing intrinsic molecular vibrations, allowing visualization without the need of exogenous labeling. Compared with fluorescence microscopy, coherent nonlinear vibrational microscopy eliminates the need for fluorescent dyes and enables live-cell and long-term dynamic observation. Its label-free chemical specificity and 3D sectioning capability offer unique application potential in medical diagnostics and materials characterization. Beyond label-free operation, a complementary direction has emerged in which vibrational probes, such as isotopic substitutions and

biorthogonal vibrational tags, are introduced to enhance sensitivity, specificity, and multiplexing capability. Unlike fluorescent labels, vibrational labels are compact, non-photobleaching, and occupy narrow spectral bands, enabling highly multiplexed imaging and quantitative molecular tracking without spectral crowding.

Despite rapid progress, several challenges remain. For instance, the limited penetration depth of light still restricts three-dimensional imaging in highly scattering living tissues. The penetration depth of nonlinear vibrational microscopy is primarily limited by optical scattering, absorption, and wavefront aberration in complex biological tissues. Nonlinear signal generation relies critically on ballistic photons and peak power at the laser foci. As the excitation beam propagates through tissue, multiscale optical scattering causes the laser intensity to attenuate approximately exponentially with depth. At the same time, the cumulative phase errors introduced by repeated scattering events progressively destroy the spatial coherence of the incident wavefront. In addition, refractive-index heterogeneity associated with microstructural constituents such as lipids and cytoplasm introduces complex wavefront distortions. As a result, the beam no longer forms a well-defined diffraction-limited focus but instead gives rise to random interference speckles at the focal plane. This focal degradation not only reduces the effective excitation intensity within the focal volume but also markedly compromises both lateral and axial resolution. One possible route is to shift the excitation wavelength toward the longer wavelength infrared window. In parallel, adaptive optics and computational wavefront correction are being explored to compensate for sample-induced aberrations.

Meanwhile, improving detection sensitivity for low-abundance molecules continues to be a critical bottleneck of coherent nonlinear vibrational microscopy. Most existing sensitivity-enhancement approaches rely on highly specific photophysical conditions, specialized nanostructures, or tailored molecular probes, which restrict their generality across diverse biological environments. At the instrumentation level, nonlinear vibrational imaging still depends on multi-laser architectures, high modulation bandwidths, and shot-noise-limited detection, which complicate system integration, portability, and deployment. Even with improved sensitivity, the achievable field of view, volumetric imaging speed, and spectral dimensionality remain mutually constrained by laser power, scanning rate, and photon budget. For clinical translation, although CRS holds significant diagnostic potential, it still faces multiple challenges at the hardware, algorithmic, and regulatory levels. First, there is a trade-off in system portability: conventional CRS systems rely on bulky solid-state lasers that are highly sensitive to environmental perturbations and thus poorly suited for the dynamic conditions of operating rooms. In contrast, fiber-based laser systems offer improved compactness and stability, but their high relative intensity noise (RIN) reduces imaging sensitivity, making it difficult to miniaturize the system without performance loss. Second, there are challenges in diagnostic reliability and interpretability. As AI becomes increasingly central to label-free histological analysis, the black-box nature of deep learning models and the risk of hallucinations in generative algorithms raise important concerns for clinical safety. Many high-performing CRS-AI methods are inherently generative and rely on learned priors that do not explicitly incorporate the underlying physical principles. In the absence of physics-informed constraints, clinicians lack a principled basis for determining whether an AI-enhanced feature reflects a genuine subtle biochemical characteristic or an artifact introduced by the model. Finally, regulatory hurdles represent a fundamental barrier to translation. As an emerging imaging modality, CRS must navigate complex approval pathways and demonstrate both safety and equivalence to current gold standards (e.g., H&E staining) through rigorous clinical validation.

Taken together, these limitations suggest that the next phase of progress will require not just incremental improvements to existing enhancement mechanisms but a broader shift toward unified optical–computational design, standardized quantitative calibration, and biologically compatible architectures that operate without restrictive substrates, high excitation power, or probe-specific tuning. The long-term goal is, therefore, not only to make nonlinear vibrational imaging more sensitive but also more generalizable, scalable, and deployable in real biological and clinical settings.

ACKNOWLEDGMENTS

We acknowledge financial support from the National Key R&D Program of China (2021YFF0502900); the National Natural Science Foundation of China (62425501); the Municipal Natural Science Foundation of Shanghai (23dz2260100); the Strategic Priority Research Program of the Chinese Academy of Sciences (XDB0650000); and the Shanghai Key Laboratory of Female Reproductive Endocrine Related Diseases.

AUTHOR DECLARATIONS

Conflict of Interest

The authors have no conflicts to disclose.

Author Contributions

Kuan Luo: Validation (equal); Visualization (equal); Writing – original draft (equal). **Dongsheng Hu:** Validation (equal); Visualization (equal); Writing – original draft (equal). **Jiaying Li:** Visualization (equal); Writing – original draft (equal). **Yue Yu:** Validation (equal). **Ke Xue:** Conceptualization (equal). **Yuan Ji:** Conceptualization (equal); Supervision (equal). **Fan Yang:** Conceptualization (equal); Writing – review & editing (equal). **Jianpeng Ao:** Conceptualization (equal); Writing – review & editing (equal). **Minbiao Ji:** Conceptualization (equal); Supervision (equal); Writing – review & editing (equal).

DATA AVAILABILITY

Data sharing is not applicable to this article as no new data were created or analyzed in this study.

REFERENCES

[1]S. W. Hell, "Far-field optical nanoscopy," Science **316**, 1153–1158 (2007).
[2]F. Zernike, "Phase contrast, a new method for the microscopic observation of transparent objects," Physica **9**, 686–698 (1942).
[3]J. W. Lichtman and J.-A. Conchello, "Fluorescence microscopy," Nat. Methods **2**, 910–919 (2005).
[4]R. Y. Tsien, "The green fluorescent protein," Annu. Rev. Biochem. **67**, 509–544 (1998).
[5]W. Denk, J. H. Strickler, and W. W. Webb, "Two-photon laser scanning fluorescence microscopy," Science **248**, 73–76 (1990).

[6]N. G. Horton, K. Wang, D. Kobat, C. G. Clark, F. W. Wise, C. B. Schaffer, and C. Xu, "In vivo three-photon microscopy of subcortical structures within an intact mouse brain," Nat. Photonics **7**, 205–209 (2013).
[7]J. Huisken, J. Swoger, F. Del Bene, J. Wittbrodt, and E. H. K. Stelzer, "Optical sectioning deep inside live embryos by selective plane illumination microscopy," Science **305**, 1007–1009 (2004).
[8]M. J. Rust, M. Bates, and X. Zhuang, "Sub-diffraction-limit imaging by stochastic optical reconstruction microscopy (STORM)," Nat. Methods **3**, 793–796 (2006).
[9]E. Betzig, G. H. Patterson, R. Sougrat, O. W. Lindwasser, S. Olenych, J. S. Bonifacino, M. W. Davidson, J. Lippincott-Schwartz, and H. F. Hess, "Imaging intracellular fluorescent proteins at nanometer resolution," Science **313**, 1642–1645 (2006).
[10]B. Huang, "Super-resolution optical microscopy: Multiple choices," Curr. Opin. Chem. Biol. **14**, 10–14 (2010).
[11]L. D. Lavis and R. T. Raines, "Bright ideas for chemical biology," ACS Chem. Biol. **3**, 142–155 (2008).
[12]M. Fernández-Suárez and A. Y. Ting, "Fluorescent probes for super-resolution imaging in living cells," Nat. Rev. Mol. Cell Biol. **9**, 929–943 (2008).
[13]G. D. E. Smith,., *Modern Raman Spectroscopy – A Practical Approach* (John Wiley & Sons, 2004), Vol. 1, pp. 1–21.
[14]J. Haas and B. Mizaikoff, "Advances in mid-infrared spectroscopy for chemical analysis," Annu. Rev. Anal. Chem. **9**, 45–68 (2016).
[15]C. H. Camp, Jr. and M. T. Cicerone, "Chemically sensitive bioimaging with coherent Raman scattering," Nat. Photonics **9**, 295–305 (2015).
[16]M. J. Baker, J. Trevisan, P. Bassan, R. Bhargava, H. J. Butler, K. M. Dorling, P. R. Fielden, S. W. Fogarty, N. J. Fullwood, K. A. Heys, C. Hughes, P. Lasch, P. L. Martin-Hirsch, B. Obinaju, G. D. Sockalingum, J. Sulé-Suso, R. J. Strong, M. J. Walsh, B. R. Wood, P. Gardner, and F. L. Martin, "Using Fourier transform IR spectroscopy to analyze biological materials," Nat. Protoc. **9**, 1771–1791 (2014).
[17]R. Bhargava, "Infrared spectroscopic imaging: The next generation," Appl. Spectrosc. **66**, 1091–1120 (2012).
[18]C. Y. Chung and E. O. Potma, "Biomolecular imaging with coherent nonlinear vibrational microscopy," Annu. Rev. Phys. Chem. **64**, 77–99 (2013).
[19]J.-X. Cheng, Y. Yuan, H. Ni, J. Ao, Q. Xia, R. Bolarinho, and X. Ge, "Advanced vibrational microscopes for life science," Nat. Methods **22**, 912–927 (2025).
[20]C. W. Ballmann, J. V. Thompson, A. J. Traverso, Z. Meng, M. O. Scully, and V. V. Yakovlev, "Stimulated Brillouin scattering microscopic imaging," Sci. Rep. **5**, 18139 (2015).
[21]L. Dalton, P. Sullivan, and A. K.-Y. Jen, *The Handbook of Photonics*, 2nd ed. (CRC Press, 2006), pp. 7-1–7-126.
[22]E. C. Y. Yan, L. Fu, Z. Wang, and W. Liu, "Biological macromolecules at interfaces probed by chiral vibrational sum frequency generation spectroscopy," Chem. Rev. **114**, 8471–8498 (2014).
[23]B. Yang, J. Ren, C.-C. Yu, Z. Wang, M. Cao, S. E. Wang, and W. Xiong, "Mode-specific coherent interference of vibrational sum-frequency generation imaging: An approach to differentiate lung tumors through collagen interfibrillar distances," J. Am. Chem. Soc. **147**, 36657–36668 (2025).
[24]J.-X. Cheng and X. S. Xie, *Coherent Raman Scattering Microscopy* (CRC Press, 2013), Vol. 1, pp. 4–41.
[25]M. E. Durst, G. Zhu, and C. Xu, "Simultaneous spatial and temporal focusing in nonlinear microscopy," Opt. Commun. **281**, 1796–1805 (2008).
[26]W. E. Moerner and D. P. Fromm, "Methods of single-molecule fluorescence spectroscopy and microscopy," Rev. Sci. Instrum. **74**, 3597–3619 (2003).
[27]Y. R. Shen, "Surface properties probed by second-harmonic and sum-frequency generation," Nature **337**, 519–525 (1989).
[28]M. Flörsheimer, C. Brillert, and H. Fuchs, "Chemical imaging of interfaces by sum frequency microscopy," Langmuir **15**, 5437–5439 (1999).
[29]D. M. P. Hoffmann, K. Kuhnke, and K. Kern, "Sum-frequency generation microscope for opaque and reflecting samples," Rev. Sci. Instrum. **73**, 3221–3226 (2002).
[30]K. Kuhnke, D. M. P. Hoffmann, X. C. Wu, A. M. Bittner, and K. Kern, "Chemical imaging of interfaces by sum-frequency generation microscopy: Application to patterned self-assembled monolayers," Appl. Phys. Lett. **83**, 3830–3832 (2003).
[31]G. Mizutani, T. Koyama, S. Tomizawa, and H. Sano, "Distinction between some saccharides in scattered optical sum frequency intensity images," Spectrochim. Acta, Part A **62**, 845–849 (2005).
[32]K. Locharoenrat, H. Sano, and G. Mizutani, "Demonstration of confocal sum frequency microscopy," Phys. Status Solidi C **6**, 304–306 (2009).
[33]K. Inoue, M. Fujii, and M. Sakai, "Development of a non-scanning vibrational sum-frequency generation detected infrared super-resolution microscope and its application to biological cells," Appl. Spectrosc. **64**, 275–281 (2010).
[34]X. Cai, B. Hu, T. Sun, K. F. Kelly, and S. Baldelli, "Sum frequency generation-compressive sensing microscope," J. Chem. Phys. **135**, 194202 (2011).
[35]D. Zheng, L. Lu, Y. Li, K. F. Kelly, and S. Baldelli, "Compressive broad-band hyperspectral sum frequency generation microscopy to study functionalized surfaces," J. Phys. Chem. Lett. **7**, 1781–1787 (2016).
[36]V. Raghunathan, Y. Han, O. Korth, N.-H. Ge, and E. O. Potma, "Rapid vibrational imaging with sum frequency generation microscopy," Opt. Lett. **36**, 3891–3893 (2011).
[37]A. Hanninen, M. W. Shu, and E. O. Potma, "Hyperspectral imaging with laser-scanning sum-frequency generation microscopy," Biomed. Opt. Express **8**, 4230–4242 (2017).
[38]N. Ji, K. Zhang, H. Yang, and Y.-R. Shen, "Three-dimensional chiral imaging by sum-frequency generation," J. Am. Chem. Soc. **128**, 3482–3483 (2006).
[39]Y. Han, V. Raghunathan, R.-R. Feng, H. Maekawa, C.-Y. Chung, Y. Feng, E. O. Potma, and N.-H. Ge, "Mapping molecular orientation with phase sensitive vibrationally resonant sum-frequency generation microscopy," J. Phys. Chem. B **117**, 6149–6156 (2013).
[40]Y. Han, J. Hsu, N.-H. Ge, and E. O. Potma, "Polarization-sensitive sum-frequency generation microscopy of collagen fibers," J. Phys. Chem. B **119**, 3356–3365 (2015).
[41]H. Wang, T. Gao, and W. Xiong, "Self-phase-stabilized heterodyne vibrational sum frequency generation microscopy," ACS Photonics **4**, 1839–1845 (2017).
[42]Z. Ji, W. Yu, D. Dong, H. Yang, K. Liu, Y.-F. Xiao, Q. Gong, Q. Song, and K. Shi, "High spatial resolution collinear chiral sum-frequency generation microscopy," AP Nexus **3**, 026006 (2024).
[43]S. A. Shah and S. Baldelli, "Chemical imaging of surfaces with sum frequency generation vibrational spectroscopy," Acc. Chem. Res. **53**, 1139–1150 (2020).
[44]J. C. Wagner, Z. Wu, H. Wang, and W. Xiong, "Imaging orientation of a single molecular hierarchical self-assembled sheet: The combined power of a vibrational sum frequency generation microscopy and neural network," J. Phys. Chem. B **126**, 7192–7201 (2022).
[45]M. Fang and S. Baldelli, "Grain structures and boundaries on microcrystalline copper covered with an octadecanethiol monolayer revealed by sum frequency generation microscopy," J. Phys. Chem. Lett. **6**, 1454–1460 (2015).
[46]H. Wang, J. C. Wagner, W. Chen, C. Wang, and W. Xiong, "Spatially dependent H-bond dynamics at interfaces of water/biomimetic self-assembled lattice materials," Proc. Natl. Acad. Sci. U. S. A. **117**, 23385–23392 (2020).
[47]I. Rocha-Mendoza, D. R. Yankelevich, M. Wang, K. M. Reiser, C. W. Frank, and A. Knoesen, "Sum frequency vibrational spectroscopy: The molecular origins of the optical second-order nonlinearity of collagen," Biophys. J. **93**, 4433–4444 (2007).
[48]E. S. Lee, S.-W. Lee, J. Hsu, and E. O. Potma, "Vibrationally resonant sum-frequency generation microscopy with a solid immersion lens," Biomed. Opt. Express **5**, 2125–2134 (2014).
[49]F. Yang and S. Baldelli, "Chemical imaging of lipid segregation: Determining different length scales of heterogeneity with compressive-sensing sum frequency generation microscopy and Brewster angle microscopy," J. Phys. Chem. B **126**, 5637–5645 (2022).
[50]A. P. Fellows, B. John, M. Wolf, and M. Thämer, "Extracting the heterogeneous 3D structure of molecular films using higher dimensional SFG microscopy," J. Phys. Chem. Lett. **15**, 10849–10857 (2024).
[51]A. P. Fellows, B. John, M. Wolf, and M. Thämer, "Spiral packing and chiral selectivity in model membranes probed by phase-resolved sum-frequency generation microscopy," Nat. Commun. **15**, 3161 (2024).

[52]J. Ao, J. Huang, and M. Ji, "Stimulated Raman scattering microscopy and its applications," Laser Optoelectron. Prog. **59**, 0400001 (2022).
[53]M. D. Duncan, J. Reintjes, and T. J. Manuccia, "Scanning coherent anti-Stokes Raman microscope," Opt. Lett. **7**, 350–352 (1982).
[54]A. Zumbusch, G. R. Holtom, and X. S. Xie, "Three-dimensional vibrational imaging by coherent anti-stokes Raman scattering," Phys. Rev. Lett. **82**, 4142–4145 (1999).
[55]J.-X. Cheng, A. Volkmer, L. D. Book, and X. S. Xie, "An epi-detected coherent anti-Stokes Raman scattering (E-CARS) microscope with high spectral resolution and high sensitivity," J. Phys. Chem. B **105**, 1277–1280 (2001).
[56]A. Volkmer, J.-X. Cheng, and X. Sunney Xie, "Vibrational imaging with high sensitivity via epidetected coherent anti-Stokes Raman scattering microscopy," Phys. Rev. Lett. **87**, 023901 (2001).
[57]C. L. Evans, E. O. Potma, M. Puoris'haag, D. Côté, C. P. Lin, and X. S. Xie, "Chemical imaging of tissue in vivo with video-rate coherent anti-Stokes Raman scattering microscopy," Proc. Natl. Acad. Sci. U. S. A. **102**, 16807–16812 (2005).
[58]J.-X. Cheng, A. Volkmer, L. D. Book, and X. S. Xie, "Multiplex coherent anti-Stokes Raman scattering microspectroscopy and study of lipid vesicles," J. Phys. Chem. B **106**, 8493–8498 (2002).
[59]M. Müller and J. M. Schins, "Imaging the thermodynamic state of lipid membranes with multiplex CARS microscopy," J. Phys. Chem. B **106**, 3715–3723 (2002).
[60]G. W. H. Wurpel, J. M. Schins, and M. Müller, "Chemical specificity in three-dimensional imaging with multiplex coherent anti-Stokes Raman scattering microscopy," Opt. Lett. **27**, 1093–1095 (2002).
[61]A. Volkmer, L. D. Book, and X. S. Xie, "Time-resolved coherent anti-Stokes Raman scattering microscopy: Imaging based on Raman free induction decay," Appl. Phys. Lett. **80**, 1505–1507 (2002).
[62]T. Hellerer, A. M. K. Enejder, and A. Zumbusch, "Spectral focusing: High spectral resolution spectroscopy with broad-bandwidth laser pulses," Appl. Phys. Lett. **85**, 25–27 (2004).
[63]J. P. Ogilvie, E. Beaurepaire, A. Alexandrou, and M. Joffre, "Fourier-transform coherent anti-Stokes Raman scattering microscopy," Opt. Lett. **31**, 480–482 (2006).
[64]T. Ideguchi, S. Holzner, B. Bernhardt, G. Guelachvili, N. Picqué, and T. W. Hänsch, "Coherent Raman spectro-imaging with laser frequency combs," Nature **502**, 355–358 (2013).
[65]Charles H. C. J., Lee Y. J., Heddleston J. M., Hartshorn C. M., Walker A. R. H., Rich J. N., Lathia J. D., and Cicerone, M. T., "High-speed coherent Raman fingerprint imaging of biological tissues," Nat. Photonics **8**, 627–634 (2014).
[66]C. Heinrich, S. Bernet, and M. Ritsch-Marte, "Wide-field coherent anti-Stokes Raman scattering microscopy," Appl. Phys. Lett. **84**, 816–818 (2004).
[67]I. Toytman, K. Cohn, T. Smith, D. Simanovskii, and D. Palanker, "Wide-field coherent anti-Stokes Raman scattering microscopy with non-phase-matching illumination," Opt. Lett. **32**, 1941–1943 (2007).
[68]C. Heinrich, A. Hofer, S. Bernet, and M. Ritsch-Marte, "Coherent anti-Stokes Raman scattering microscopy with dynamic speckle illumination," New J. Phys. **10**, 023029 (2008).
[69]M. Lei, M. Winterhalder, R. Selm, and A. Zumbusch, "Video-rate wide-field coherent anti-Stokes Raman scattering microscopy with collinear nonphase-matching illumination," J. Biomed. Opt. **16**, 021102 (2011).
[70]P. Berto, D. Gachet, P. Bon, S. Monneret, and H. Rigneault, "Wide-field vibrational phase imaging," Phys. Rev. Lett. **109**, 093902 (2012).
[71]C. Zong, R. Cheng, F. Chen, P. Lin, M. Zhang, Z. Chen, C. Li, C. Yang, and J.-X. Cheng, "Wide-field surface-enhanced coherent anti-Stokes Raman scattering microscopy," ACS Photonics **9**, 1042–1049 (2022).
[72]E. M. Fantuzzi, S. Heuke, S. Labouesse, D. Gudavičius, R. Bartels, A. Sentenac, and H. Rigneault, "Wide-field coherent anti-Stokes Raman scattering microscopy using random illuminations," Nat. Photonics **17**, 1097–1104 (2023).
[73]L. Gong, W. Zheng, Y. Ma, and Z. Huang, "Higher-order coherent anti-Stokes Raman scattering microscopy realizes label-free super-resolution vibrational imaging," Nat. Photonics **14**, 115–122 (2020).
[74]X. Nan, J.-X. Cheng, and X. S. Xie, "Vibrational imaging of lipid droplets in live fibroblast cells with coherent anti-Stokes Raman scattering microscopy," J. Lipid Res. **44**, 2202–2208 (2003).
[75]M. Paar, C. Jüngst, N. A. Steiner, C. Magnes, F. Sinner, D. Kolb, A. Lass, R. Zimmermann, A. Zumbusch, S. D. Kohlwein, and H. Wolinski, "Remodeling of lipid droplets during lipolysis and growth in adipocytes," J. Biol. Chem. **287**, 11164–11173 (2012).
[76]T. T. Le, T. B. Huff, and J.-X. Cheng, "Coherent anti-Stokes Raman scattering imaging of lipids in cancer metastasis," BMC Cancer **9**, 42 (2009).
[77]R. Mitra, O. Chao, Y. Urasaki, O. B. Goodman, and T. T. Le, "Detection of lipid-rich prostate circulating tumour cells with coherent anti-Stokes Raman scattering microscopy," BMC Cancer **12**, 540 (2012).
[78]M. Okuno, H. Kano, K. Fujii, K. Bito, S. Naito, P. Leproux, V. Couderc, and H.-O. Hamaguchi, "Surfactant uptake dynamics in mammalian cells elucidated with quantitative coherent anti-stokes Raman scattering microspectroscopy," PLoS One **9**, e93401 (2014).
[79]C. Di Napoli, I. Pope, F. Masia, P. Watson, W. Langbein, and P. Borri, "Hyperspectral and differential CARS microscopy for quantitative chemical imaging in human adipocytes," Biomed. Opt. Express **5**, 1378–1390 (2014).
[80]T. B. Huff and J.-X. Cheng, "In vivo coherent anti-Stokes Raman scattering imaging of sciatic nerve tissue," J. Microsc. **225**, 175–182 (2007).
[81]Y. Shi, D. Zhang, T. B. Huff, X. Wang, R. Shi, X.-M. Xu, and J.-X. Cheng, "Longitudinal in vivo coherent anti-Stokes Raman scattering imaging of demyelination and remyelination in injured spinal cord," J. Biomed. Opt. **16**, 106012 (2011).
[82]H.-W. Wang, I. M. Langohr, M. Sturek, and J.-X. Cheng, "Imaging and quantitative analysis of atherosclerotic lesions by CARS-based multimodal nonlinear optical microscopy," Arterioscler., Thromb., Vasc. Biol. **29**, 1342–1348 (2009).
[83]R. S. Lim, J. L. Suhalim, S. Miyazaki-Anzai, M. Miyazaki, M. Levi, E. O. Potma, and B. J. Tromberg, "Identification of cholesterol crystals in plaques of atherosclerotic mice using hyperspectral CARS imaging," J. Lipid Res. **52**, 2177–2186 (2011).
[84]L. B. Mostaço-Guidolin, M. G. Sowa, A. Ridsdale, A. F. Pegoraro, M. S. D. Smith, M. D. Hewko, E. K. Kohlenberg, B. Schattka, M. Shiomi, A. Stolow, and A. C. T. Ko, "Differentiating atherosclerotic plaque burden in arterial tissues using femtosecond CARS-based multimodal nonlinear optical imaging," Biomed. Opt. Express **1**, 59–73 (2010).
[85]N. Kiss, Á. Krolopp, K. Lőrincz, A. Bánvölgyi, R. Szipőcs, and N. Wikonkál, "Stain-free histopathology of basal cell carcinoma by dual vibration resonance frequency CARS microscopy," Pathol. Oncol. Res. **24**, 927–930 (2018).
[86]W.-W. Chen, G. A. Lemieux, C. H. Camp, T.-C. Chang, K. Ashrafi, and M. T. Cicerone, "Spectroscopic coherent Raman imaging of *Caenorhabditis elegans* reveals lipid particle diversity," Nat. Chem. Biol. **16**, 1087–1095 (2020).
[87]O. Chernavskaia, S. Heuke, M. Vieth, O. Friedrich, S. Schürmann, R. Atreya, A. Stallmach, M. F. Neurath, M. Waldner, I. Petersen, M. Schmitt, T. Bocklitz, and J. Popp, "Beyond endoscopic assessment in inflammatory bowel disease: Real-time histology of disease activity by non-linear multimodal imaging," Sci. Rep. **6**, 29239 (2016).
[88]B. von Vacano, L. Meyer, and M. Motzkus, "Rapid polymer blend imaging with quantitative broadband multiplex CARS microscopy," J. Raman Spectrosc. **38**, 916–926 (2007).
[89]M. H. F. Kox, K. F. Domke, J. P. R. Day, G. Rago, E. Stavitski, M. Bonn, and B. M. Weckhuysen, "Label-free chemical imaging of catalytic solids by coherent anti-Stokes Raman scattering and synchrotron-based infrared microscopy," Angew. Chem., Int. Ed. **48**, 8990–8994 (2009).
[90]S. Heuke and H. Rigneault, "Coherent Stokes Raman scattering microscopy (CSRS)," Nat. Commun. **14**, 3337 (2023).
[91]W. Min, J.-X. Cheng, and Y. Ozeki, "Theory, innovations and applications of stimulated Raman scattering microscopy," Nat. Photonics **19**, 803–816 (2025).
[92]E. Ploetz, S. Laimgruber, S. Berner, W. Zinth, and P. Gilch, "Femtosecond stimulated Raman microscopy," Appl. Phys. B **87**, 389–393 (2007).
[93]C. W. Freudiger, W. Min, B. G. Saar, S. Lu, G. R. Holtom, C. He, J. C. Tsai, J. X. Kang, and X. S. Xie, "Label-free biomedical imaging with high sensitivity by stimulated Raman scattering microscopy," Science **322**, 1857–1861 (2008).
[94]Y. Ozeki, W. Umemura, K. Sumimura, N. Nishizawa, K. Fukui, and K. Itoh, "Stimulated Raman hyperspectral imaging based on spectral filtering of broadband fiber laser pulses," Opt. Lett. **37**, 431–433 (2012).

[95]S. Karpf, M. Eibl, W. Wieser, T. Klein, and R. Huber, "A Time-Encoded Technique for fibre-based hyperspectral broadband stimulated Raman microscopy," Nat. Commun. **6**, 6784 (2015).
[96]M. Brinkmann, A. Fast, T. Hellwig, I. Pence, C. L. Evans, and C. Fallnich, "Portable all-fiber dual-output widely tunable light source for coherent Raman imaging," Biomed. Opt. Express **10**, 4437–4449 (2019).
[97]H. Ni, P. Lin, Y. Zhu, M. Zhang, Y. Tan, Y. Zhan, Z. Wang, and J.-X. Cheng, "Multiwindow SRS imaging using a rapid widely tunable fiber laser," Anal. Chem. **93**, 15703–15711 (2021).
[98]E. R. Andresen, P. Berto, and H. Rigneault, "Stimulated Raman scattering microscopy by spectral focusing and fiber-generated soliton as Stokes pulse," Opt. Lett. **36**, 2387–2389 (2011).
[99]C. S. Liao, K. C. Huang, W. Hong, J. Chen, K. Caroline, G. Eakins, and J.-X. Cheng, "Stimulated Raman spectroscopic imaging by microsecond delay-line tuning," in *2016 Asia Communications and Photonics Conference (ACP)* (IEEE, 2016), pp. 1–2.
[100]H. Lin, H. J. Lee, N. Tague, J.-B. Lugagne, C. Zong, F. Deng, J. Shin, L. Tian, W. Wong, M. J. Dunlop, and J.-X. Cheng, "Microsecond fingerprint stimulated Raman spectroscopic imaging by ultrafast tuning and spatial-spectral learning," Nat. Commun. **12**, 3052 (2021).
[101]M. S. Alshaykh, C.-S. Liao, O. E. Sandoval, G. Gitzinger, N. Forget, D. E. Leaird, J.-X. Cheng, and A. M. Weiner, "High-speed stimulated hyperspectral Raman imaging using rapid acousto-optic delay lines," Opt. Lett. **42**, 1548 (2017).
[102]D. Fu, F.-K. Lu, X. Zhang, C. Freudiger, D. R. Pernik, G. Holtom, and X. S. Xie, "Quantitative chemical imaging with multiplex stimulated Raman scattering microscopy," J. Am. Chem. Soc. **134**, 3623–3626 (2012).
[103]C.-S. Liao, M. N. Slipchenko, P. Wang, J. Li, S.-Y. Lee, R. A. Oglesbee, and J.-X. Cheng, "Microsecond scale vibrational spectroscopic imaging by multiplex stimulated Raman scattering microscopy," Light: Sci. Appl. **4**, e265 (2015).
[104]C.-S. Liao, P. Wang, P. Wang, J. Li, H. J. Lee, G. Eakins, and J.-X. Cheng, "Spectrometer-free vibrational imaging by retrieving stimulated Raman signal from highly scattered photons," Sci. Adv. **1**, e1500738 (2015).
[105]J. Réhault, F. Crisafi, V. Kumar, G. Ciardi, M. Marangoni, G. Cerullo, and D. Polli, "Broadband stimulated Raman scattering with Fourier-transform detection," Opt. Express **23**, 25235–25246 (2015).
[106]R. He, Y. Xu, L. Zhang, S. Ma, X. Wang, D. Ye, and M. Ji, "Dual-phase stimulated Raman scattering microscopy for real-time two-color imaging," Optica **4**, 44–47 (2017).
[107]B. Zhang, M. Sun, Y. Yang, L. Chen, X. Zou, T. Yang, Y. Hua, and M. Ji, "Rapid, large-scale stimulated Raman histology with strip mosaicing and dual-phase detection," Biomed. Opt. Express **9**, 2604–2613 (2018).
[108]Q. Yu, Z. Yao, J. Zhou, W. Yu, C. Zhuang, Y. Qi, and H. Xiong, "Transient stimulated Raman scattering spectroscopy and imaging," Light: Sci. Appl. **13**, 70 (2024).
[109]J. Guo, M. Wang, Q. Yu, H. Zhang, J. Wang, Q. Zhang, Y. Qi, Z. Wang, J. Liu, H. Sun, J. Ren, X. Zhang, W. Yu, X. Yu, W. Si, and H. Xiong, "Super-broadband stimulated Raman scattering spectroscopy and imaging," Nat. Photonics **20**, 444 (2026).
[110]L. Wei, Z. Chen, L. Shi, R. Long, A. V. Anzalone, L. Zhang, F. Hu, R. Yuste, V. W. Cornish, and W. Min, "Super-multiplex vibrational imaging," Nature **544**, 465–470 (2017).
[111]C. Zong, R. Premasiri, H. Lin, Y. Huang, C. Zhang, C. Yang, B. Ren, L. D. Ziegler, and J.-X. Cheng, "Plasmon-enhanced stimulated Raman scattering microscopy with single-molecule detection sensitivity," Nat. Commun. **10**, 5318 (2019).
[112]M. Zhuge, K. C. Huang, H. J. Lee, Y. Jiang, Y. Tan, H. Lin, P. T. Dong, G. Zhao, D. Matei, Q. Yang, and J. X. Cheng, "Ultrasensitive vibrational imaging of retinoids by visible preresonance stimulated Raman scattering microscopy," Adv. Sci. **8**, 2003136 (2021).
[113]H. Lin, S. Seitz, Y. Tan, J.-B. Lugagne, L. Wang, G. Ding, H. He, T. J. Rauwolf, M. J. Dunlop, J. H. Connor, J. A. Porco, L. Tian, and J.-X. Cheng, "Label-free nanoscopy of cell metabolism by ultrasensitive reweighted visible stimulated Raman scattering," Nat. Methods **22**, 1040 (2025).
[114]S. Oh, Y. Eom, H. Y. Kim, A. Tripathi, S. Park, H. Y. Woo, and S.-H. Shim, "Fluorescence-free single-molecule microscopy via electronic resonance stimulated Raman scattering," Nat. Commun. **17**, 2720 (2026).
[115]Y. Bi, C. Yang, Y. Chen, S. Yan, G. Yang, Y. Wu, G. Zhang, and P. Wang, "Near-resonance enhanced label-free stimulated Raman scattering microscopy with spatial resolution near 130 nm," Light: Sci. Appl. **7**, 81 (2018).
[116]L. Gong and H. Wang, "Breaking the diffraction limit by saturation in stimulated-Raman-scattering microscopy: A theoretical study," Phys. Lett. A **90**, 013818 (2014).
[117]W. R. Silva, C. T. Graefe, and R. R. Frontiera, "Toward label-free super-resolution microscopy," ACS Photonics **3**, 79–86 (2016).
[118]H. Xiong, N. Qian, Y. Miao, Z. Zhao, C. Chen, and W. Min, "Super-resolution vibrational microscopy by stimulated Raman excited fluorescence," Light: Sci. Appl. **10**, 87 (2021).
[119]J. Ao, X. Fang, L. Ma, Z. Liu, S. Wu, C. Wu, and M. Ji, "Photoswitchable vibrational nanoscopy with sub-100-nm optical resolution," Adv. Photonics **5**, 066001 (2023).
[120]J. Shou, A. Komazawa, Y. Wachi, M. Kawatani, H. Fujioka, S. J. Spratt, T. Mizuguchi, K. Oguchi, H. Akaboshi, F. Obata, R. Tachibana, S. Yasunaga, Y. Mita, Y. Misawa, R. Kojima, Y. Urano, M. Kamiya, and Y. Ozeki, "Super-resolution vibrational imaging based on photoswitchable Raman probe," Sci. Adv. **9**, eade9118 (2023).
[121]C. Qian, K. Miao, L.-E. Lin, X. Chen, J. Du, and L. Wei, "Super-resolution label-free volumetric vibrational imaging," Nat. Commun. **12**, 3648 (2021).
[122]L. Shi, A. Klimas, B. Gallagher, Z. Cheng, F. Fu, P. Wijesekara, Y. Miao, X. Ren, Y. Zhao, and W. Min, "Super-resolution vibrational imaging using expansion stimulated Raman scattering microscopy," Adv. Sci. **9**, 2200315 (2022).
[123]J. I. Kim, Z. Ellsworth, E. L. Dunnington, B. S. Wong, N. R. Mehta, C. Zensho, and D. Fu, "4Pi stimulated Raman scattering for label-free super-resolution chemical imaging," Sci. Adv. **12**, eaec0523 (2026).
[124]H. Jang, Y. Li, A. A. Fung, P. Bagheri, K. Hoang, D. Skowronska-Krawczyk, X. Chen, J. Y. Wu, B. Bintu, and L. Shi, "Super-resolution SRS microscopy with A-PoD," Nat. Methods **20**, 448–458 (2023).
[125]X. Chen, C. Zhang, P. Lin, K.-C. Huang, J. Liang, J. Tian, and J.-X. Cheng, "Volumetric chemical imaging by stimulated Raman projection microscopy and tomography," Nat. Commun. **8**, 15117 (2017).
[126]W. Wang and Z. Huang, "Stimulated Raman scattering tomography for rapid three-dimensional chemical imaging of cells and tissue," Adv. Photonics **6**, 026001 (2024).
[127]F. E. Robles, K. C. Zhou, M. C. Fischer, and W. S. Warren, "Stimulated Raman scattering spectroscopic optical coherence tomography," Optica **4**, 243–246 (2017).
[128]M. Wei, L. Shi, Y. Shen, Z. Zhao, A. Guzman, L. J. Kaufman, L. Wei, and W. Min, "Volumetric chemical imaging by clearing-enhanced stimulated Raman scattering microscopy," Proc. Natl. Acad. Sci. U. S. A. **116**, 6608–6617 (2019).
[129]L. Shi, M. Wei, Y. Miao, N. Qian, L. Shi, R. A. Singer, R. K. P. Benninger, and W. Min, "Highly-multiplexed volumetric mapping with Raman dye imaging and tissue clearing," Nat. Biotechnol. **40**, 364–373 (2022).
[130]M. Ji, M. Arbel, L. Zhang, C. W. Freudiger, S. S. Hou, D. Lin, X. Yang, B. J. Bacskai, and X. S. Xie, "Label-free imaging of amyloid plaques in Alzheimer's disease with stimulated Raman scattering microscopy," Sci. Adv. **4**, eaat7715 (2018).
[131]H. J. Lee, D. Zhang, Y. Jiang, X. Wu, P.-Y. Shih, C.-S. Liao, B. Bungart, X.-M. Xu, R. Drenan, E. Bartlett, and J.-X. Cheng, "Label-free vibrational spectroscopic imaging of neuronal membrane potential," J. Phys. Chem. Lett. **8**, 1932–1936 (2017).
[132]F.-K. Lu, S. Basu, V. Igras, M. P. Hoang, M. Ji, D. Fu, G. R. Holtom, V. A. Neel, C. W. Freudiger, D. E. Fisher, and X. S. Xie, "Label-free DNA imaging in vivo with stimulated Raman scattering microscopy," Proc. Natl. Acad. Sci. U. S. A. **112**, 11624–11629 (2015).
[133]J. Zhang, H. Lin, J. Xu, M. Zhang, X. Ge, C. Zhang, W. E. Huang, and J.-X. Cheng, "High-throughput single-cell sorting by stimulated Raman-activated cell ejection," Sci. Adv. **10**, eadn6373 (2024).
[134]R. Sun, Y. Zhuang, Y. Lin, and F. Hu, "In situ secondary structure imaging of protein phase separation and aggregation by hyperspectral stimulated Raman scattering microscopy," Nat. Commun. **16**, 8552 (2025).
[135]Y. Shen, Z. Zhao, L. Zhang, L. Shi, S. Shahriar, R. B. Chan, G. Di Paolo, and W. Min, "Metabolic activity induces membrane phase separation in endoplasmic reticulum," Proc. Natl. Acad. Sci. U. S. A. **114**, 13394–13399 (2017).

[136]C.-C. J. Lin and M. C. Wang, "Microbial metabolites regulate host lipid metabolism through NR5A–Hedgehog signalling," Nat. Cell Biol. **19**, 550–557 (2017).
[137]A. N. von Krusenstiern, R. N. Robson, N. Qian, B. Qiu, F. Hu, E. Reznik, N. Smith, F. Zandkarimi, V. M. Estes, M. Dupont, T. Hirschhorn, M. S. Shchepinov, W. Min, K. A. Woerpel, and B. R. Stockwell, "Identification of essential sites of lipid peroxidation in ferroptosis," Nat. Chem. Biol. **19**, 719–730 (2023).
[138]L. Zhang, L. Shi, Y. Shen, Y. Miao, M. Wei, N. Qian, Y. Liu, and W. Min, "Spectral tracing of deuterium for imaging glucose metabolism," Nat. Biomed. Eng. **3**, 402–413 (2019).
[139]S. Bi, J. Ao, T. Jiang, X. Zhu, Y. Zhu, W. Yang, B. Zheng, and M. Ji, "imaging metabolic flow of water in plants with isotope-traced stimulated Raman scattering microscopy," Adv. Sci. **11**, 2407543 (2024).
[140]L. Shi, C. Zheng, Y. Shen, Z. Chen, E. S. Silveira, L. Zhang, M. Wei, C. Liu, C. de Sena-Tomas, K. Targoff, and W. Min, "Optical imaging of metabolic dynamics in animals," Nat. Commun. **9**, 2995 (2018).
[141]F. Hu, C. Zeng, R. Long, Y. Miao, L. Wei, Q. Xu, and W. Min, "Supermultiplexed optical imaging and barcoding with engineered polyynes," Nat. Methods **15**, 194–200 (2018).
[142]M. Ji, D. A. Orringer, C. W. Freudiger, S. Ramkissoon, X. Liu, D. Lau, A. J. Golby, I. Norton, M. Hayashi, N. Y. R. Agar, G. S. Young, C. Spino, S. Santagata, S. Camelo-Piragua, K. L. Ligon, O. Sagher, and X. S. Xie, "Rapid, label-free detection of brain tumors with stimulated Raman scattering microscopy," Sci. Transl. Med. **5**, 201ra119 (2013).
[143]K. Bae, W. Zheng, K. Lin, S. W. Lim, Y. K. Chong, C. Tang, N. K. King, C. B. Ti Ang, and Z. Huang, "Epi-detected hyperspectral stimulated Raman Scattering microscopy for label-free molecular subtyping of glioblastomas," Anal. Chem. **90**, 10249–10255 (2018).
[144]M. Ji, S. Lewis, S. Camelo-Piragua, S. H. Ramkissoon, M. Snuderl, S. Venneti, A. Fisher-Hubbard, M. Garrard, D. Fu, A. C. Wang, J. A. Heth, C. O. Maher, N. Sanai, T. D. Johnson, C. W. Freudiger, O. Sagher, X. S. Xie, and D. A. Orringer, "Detection of human brain tumor infiltration with quantitative stimulated Raman scattering microscopy," Sci. Transl. Med. **7**, 309ra163 (2015).
[145]F.-K. Lu, D. Calligaris, O. I. Olubiyi, I. Norton, W. Yang, S. Santagata, X. S. Xie, A. J. Golby, and N. Y. R. Agar, "Label-free neurosurgical pathology with stimulated Raman imaging," Cancer Res. **76**, 3451–3462 (2016).
[146]K. S. Shin, M. Laohajaratsang, S. Men, B. Figueroa, S. M. Dintzis, and D. Fu, "Quantitative chemical imaging of breast calcifications in association with neoplastic processes," Theranostics **10**, 5865–5878 (2020).
[147]Y. Yang, Y. Yang, Z. Liu, L. Guo, S. Li, X. Sun, Z. Shao, and M. Ji, "Microcalcification-based tumor malignancy evaluation in fresh breast biopsies with hyperspectral stimulated Raman scattering," Anal. Chem. **93**, 6223–6231 (2021).
[148]Y. Yang, Z. Liu, J. Huang, X. Sun, J. Ao, B. Zheng, W. Chen, Z. Shao, H. Hu, Y. Yang, and M. Ji, "Histological diagnosis of unprocessed breast core-needle biopsy via stimulated Raman scattering microscopy and multi-instance learning," Theranostics **13**, 1342–1354 (2023).
[149]H. Ni, C. P. Dessai, H. Lin, W. Wang, S. Chen, Y. Yuan, X. Ge, J. Ao, N. Vild, and J.-X. Cheng, "High-content stimulated Raman histology of human breast cancer," Theranostics **14**, 1361–1370 (2024).
[150]Z. Liu, W. Su, J. Ao, M. Wang, Q. Jiang, J. He, H. Gao, S. Lei, J. Nie, X. Yan, X. Guo, P. Zhou, H. Hu, and M. Ji, "Instant diagnosis of gastroscopic biopsy via deep-learned single-shot femtosecond stimulated Raman histology," Nat. Commun. **13**, 4050 (2022).
[151]J. Ao, X. Shao, Z. Liu, Q. Liu, J. Xia, Y. Shi, L. Qi, J. Pan, and M. Ji, "Stimulated Raman scattering microscopy enables Gleason scoring of prostate core needle biopsy by a convolutional neural network," Cancer Res. **83**, 641–651 (2023).
[152]L. Ma, K. Luo, Z. Liu, and M. Ji, "Stain-free histopathology with stimulated Raman scattering microscopy," Anal. Chem. **96**, 7907–7925 (2024).
[153]B. Manifold, S. Men, R. Hu, and D. Fu, "A versatile deep learning architecture for classification and label-free prediction of hyperspectral images," Nat. Mach. Intell. **3**, 306–315 (2021).
[154]J. Zhang, J. Zhao, H. Lin, Y. Tan, and J.-X. Cheng, "High-speed chemical imaging by dense-net learning of femtosecond stimulated Raman scattering," J. Phys. Chem. Lett. **11**, 8573–8578 (2020).
[155]T. C. Hollon, B. Pandian, A. R. Adapa, E. Urias, A. V. Save, S. S. S. Khalsa, D. G. Eichberg, R. S. D'Amico, Z. U. Farooq, S. Lewis, P. D. Petridis, T. Marie, A. H. Shah, H. J. L. Garton, C. O. Maher, J. A. Heth, E. L. McKean, S. E. Sullivan, S. L. Hervey-Jumper, P. G. Patil, B. G. Thompson, O. Sagher, G. M. McKhann, R. J. Komotar, M. E. Ivan, M. Snuderl, M. L. Otten, T. D. Johnson, M. B. Sisti, J. N. Bruce, K. M. Muraszko, J. Trautman, C. W. Freudiger, P. Canoll, H. Lee, S. Camelo-Piragua, and D. A. Orringer, "Near real-time intraoperative brain tumor diagnosis using stimulated Raman histology and deep neural networks," Nat. Med. **26**, 52–58 (2020).
[156]D. A. Orringer, B. Pandian, Y. S. Niknafs, T. C. Hollon, J. Boyle, S. Lewis, M. Garrard, S. L. Hervey-Jumper, H. J. L. Garton, C. O. Maher, J. A. Heth, O. Sagher, D. A. Wilkinson, M. Snuderl, S. Venneti, S. H. Ramkissoon, K. A. McFadden, A. Fisher-Hubbard, A. P. Lieberman, T. D. Johnson, X. S. Xie, J. K. Trautman, C. W. Freudiger, and S. Camelo-Piragua, "Rapid intraoperative histology of unprocessed surgical specimens via fibre-laser-based stimulated Raman scattering microscopy," Nat. Biomed. Eng. **1**, 0027 (2017).
[157]L. Zhang, Y. Wu, B. Zheng, L. Su, Y. Chen, S. Ma, Q. Hu, X. Zou, L. Yao, Y. Yang, L. Chen, Y. Mao, Y. Chen, and M. Ji, "Rapid histology of laryngeal squamous cell carcinoma with deep-learning based stimulated Raman scattering microscopy," Theranostics **9**, 2541–2554 (2019).
[158]K. Falahkheirkhah, S. S. Mukherjee, S. Gupta, L. Herrera-Hernandez, M. R. McCarthy, R. E. Jimenez, J. C. Cheville, and R. Bhargava, "Accelerating cancer histopathology workflows with chemical imaging and machine learning," Cancer Res. Commun. **3**, 1875–1887 (2023).
[159]Z. Liu, L. Chen, H. Cheng, J. Ao, J. Xiong, X. Liu, Y. Chen, Y. Mao, and M. Ji, "Virtual formalin-fixed and paraffin-embedded staining of fresh brain tissue via stimulated Raman CycleGAN model," Sci. Adv. **10**, eadn3426 (2024).
[160]B. Shen, Z. Li, Y. Pan, Y. Guo, Z. Yin, R. Hu, J. Qu, and L. Liu, "Noninvasive nonlinear optical computational histology," Adv. Sci. **11**, 2308630 (2024).
[161]A. Kondepudi, M. Pekmezci, X. Hou, K. Scotford, C. Jiang, A. Rao, E. S. Harake, A. Chowdury, W. Al-Holou, L. Wang, A. Pandey, P. R. Lowenstein, M. G. Castro, L. I. Koerner, T. Roetzer-Pejrimovsky, G. Widhalm, S. Camelo-Piragua, M. Movahed-Ezazi, D. A. Orringer, H. Lee, C. Freudiger, M. Berger, S. Hervey-Jumper, and T. Hollon, "Foundation models for fast, label-free detection of glioma infiltration," Nature **637**, 439–445 (2025).
[162]L. Ma, Y. Guo, M. Du, Y. Cai, Y. He, Q. Meng, Z. Liu, Y. Lan, M. Li, M. Ji, and L. Qi, "DeepLuAd: Semantic-guided virtual histopathology of lung adenocarcinoma via stimulated Raman scattering," Theranostics **16**, 2324–2341 (2026).
[163]Y. Chen, Z. Liu, and M. Ji, "Imaging low-temperature phases of ice with polarization-resolved hyperspectral stimulated Raman scattering microscopy," J. Phys. Chem. B **127**, 2609–2616 (2023).
[164]K. Gong, J. Ao, K. Li, L. Liu, Y. Liu, G. Xu, T. Wang, H. Cheng, Z. Wang, X. Zhang, H. Wei, C. George, A. Mellouki, H. Herrmann, L. Wang, J. Chen, M. Ji, L. Zhang, and J. S. Francisco, "Imaging of pH distribution inside individual microdroplet by stimulated Raman microscopy," Proc. Natl. Acad. Sci. U. S. A. **120**, e2219588120 (2023).
[165]H. Xiong, J. K. Lee, R. N. Zare, and W. Min, "Strong electric field observed at the interface of aqueous microdroplets," J. Phys. Chem. Lett. **11**, 7423–7428 (2020).
[166]Q. Cheng, T. Jin, Y. Miao, Z. Liu, J. Borovilas, H. Zhang, S. Liu, S.-Y. Kim, R. Zhang, H. Wang, X. Chen, L.-Q. Chen, J. Li, W. Min, and Y. Yang, "Stabilizing lithium plating in polymer electrolytes by concentration-polarization-induced phase transformation," Joule **6**, 2372–2389 (2022).
[167]Q. Cheng, L. Wei, Z. Liu, N. Ni, Z. Sang, B. Zhu, W. Xu, M. Chen, Y. Miao, L.-Q. Chen, W. Min, and Y. Yang, "Operando and three-dimensional visualization of anion depletion and lithium growth by stimulated Raman scattering microscopy," Nat. Commun. **9**, 2942 (2018).
[168]H. Li, Y. Cheng, H. Tang, Y. Bi, Y. Chen, G. Yang, S. Guo, S. Tian, J. Liao, X. Lv, S. Zeng, M. Zhu, C. Xu, J.-X. Cheng, and P. Wang, "Imaging chemical kinetics of radical polymerization with an ultrafast coherent Raman microscope," Adv. Sci. **7**, 1903644 (2020).
[169]J. Ao, Y. Feng, S. Wu, T. Wang, J. Ling, L. Zhang, and M. Ji, "Rapid, 3D chemical profiling of individual atmospheric aerosols with stimulated Raman scattering microscopy," Small Methods **4**, 1900600 (2020).
[170]J. Ao, G. Xu, H. Wu, L. Xie, J. Liu, K. Gong, X. Ruan, J. Han, K. Li, W. Wang, T. Chen, M. Ji, and L. Zhang, "Fast detection and 3D imaging of nanoplastics

and microplastics by stimulated Raman scattering microscopy," Cell Rep. Phys. Sci. **4**, 101623 (2023).
[171]N. Qian, X. Gao, X. Lang, H. Deng, T. M. Bratu, Q. Chen, P. Stapleton, B. Yan, and W. Min, "Rapid single-particle chemical imaging of nanoplastics by SRS microscopy," Proc. Natl. Acad. Sci. U. S. A. **121**, e2300582121 (2024).
[172]M. Wang, Z. Huang, C. Wu, S. Yan, H.-T. Fang, W. Pan, Q.-G. Tan, K. Pan, R. Ji, L. Yang, B. Pan, P. Wang, and A.-J. Miao, "Stimulated Raman scattering microscopy reveals bioaccumulation of small microplastics in protozoa from natural waters," Environ. Sci. Technol. **58**, 2922–2930 (2024).
[173]Y. Zhu, X. Ge, H. Ni, J. Yin, H. Lin, L. Wang, Y. Tan, C. V. Prabhu Dessai, Y. Li, X. Teng, and J.-X. Cheng, "Stimulated Raman photothermal microscopy toward ultrasensitive chemical imaging," Sci. Adv. **9**, eadi2181 (2023).
[174]X. Gao, X. Li, and W. Min, "Absolute stimulated Raman cross sections of molecules," J. Phys. Chem. Lett. **14**, 5701–5708 (2023).
[175]X. Ge, Y. Zhu, D. Sun, H. Ni, Y. Li, C. V. P. Dessai, and J.-X. Cheng, "Fiber laser based stimulated Raman photothermal microscopy towards a high-performance and user-friendly chemical imaging platform," PhotoniX **6**, 35 (2025).
[176]H. Xiong, L. Shi, L. Wei, Y. Shen, R. Long, Z. Zhao, and W. Min, "Stimulated Raman excited fluorescence spectroscopy and imaging," Nat. Photonics **13**, 412–417 (2019).
[177]A. Bilenca, R. Prevedel, and G. Scarcelli, "Current state of stimulated Brillouin scattering microscopy for the life sciences," J. Phys. Photonics **6**, 032001 (2024).
[178]R. W. Boyd, *Nonlinear Optics*, 3rd ed. (Academic Press, Inc., 2008).
[179]C. Shi, H. Zhang, and J. Zhang, "Non-contact and label-free biomechanical imaging: Stimulated Brillouin microscopy and beyond," Front. Phys. **11**, 1175653 (2023).
[180]G. Scarcelli and S. H. Yun, "Confocal Brillouin microscopy for three-dimensional mechanical imaging," Nat. Photonics **2**, 39–43 (2008).
[181]I. Kabakova, J. Zhang, Y. Xiang, S. Caponi, A. Bilenca, J. Guck, and G. Scarcelli, "Brillouin microscopy," Nat. Rev. Methods Primers **4**, 8 (2024).
[182]C. Bevilacqua, J. M. Gomez, U.-M. Fiuza, C. J. Chan, L. Wang, S. Hambura, M. Eguren, J. Ellenberg, A. Diz-Muñoz, M. Leptin, and R. Prevedel, "High-resolution line-scan Brillouin microscopy for live imaging of mechanical properties during embryo development," Nat. Methods **20**, 755–760 (2023).
[183]J. Zhang, M. Nikolic, K. Tanner, and G. Scarcelli, "Rapid biomechanical imaging at low irradiation level via dual line-scanning Brillouin microscopy," Nat. Methods **20**, 677–681 (2023).
[184]C. Bevilacqua and R. Prevedel, "Full-field Brillouin microscopy based on an imaging Fourier-transform spectrometer," Nat. Photonics **19**, 494–501 (2025).
[185]Y. Qi, S. Yao, Z.-X. Du, J.-R. Zhang, C. Zhou, X. Fu, H. Li, T. Mi, Y.-H. Chen, Y.-F. Wang, Y. Luo, X. He, J. Nan, Y. Zhang, L. Sun, P. Xia, S.-Q. Cai, J.-L. Du, J. Xie, W.-B. Chen, and F. Yang, "Stimulated Brillouin scattering microscopy with a high-peak-power 780-nm pulsed laser system," Nat. Photonics **19**, 879 (2025).
[186]R. Prevedel, A. Diz-Muñoz, G. Ruocco, and G. Antonacci, "Brillouin microscopy: An emerging tool for mechanobiology," Nat. Methods **16**, 969–977 (2019).
[187]K. A. Nelson and M. D. Fayer, "Laser induced phonons: A probe of intermolecular interactions in molecular solids," J. Chem. Phys. **72**, 5202–5218 (1980).
[188]C. Y. She, G. C. Herring, H. Moosmüller, and S. A. Lee, "Stimulated Rayleigh-Brillouin gain spectroscopy," Phys. Rev. A **31**, 3733–3740 (1985).
[189]S. Y. Tang, C. Y. She, and S. A. Lee, "Continuous-wave Rayleigh–Brillouin-gain spectroscopy in SF6," Opt. Lett. **12**, 870–872 (1987).
[190]G. W. Faris, L. E. Jusinski, M. J. Dyer, W. K. Bischel, and A. P. Hickman, "High-resolution Brillouin gain spectroscopy in fused silica," Opt. Lett. **15**, 703–705 (1990).
[191]K. Ratanaphruks, W. Tandy Grubbs, and R. A. MacPhail, "CW stimulated Brillouin gain spectroscopy of liquids," Chem. Phys. Lett. **182**, 371–378 (1991).
[192]S. Kinoshita, Y. Shimada, W. Tsurumaki, M. Yamaguchi, and T. Yagi, "New high-resolution phonon spectroscopy using impulsive stimulated Brillouin scattering," Rev. Sci. Instrum. **64**, 3384–3393 (1993).
[193]I. Remer and A. Bilenca, "Background-free Brillouin spectroscopy in scattering media at 780 nm via stimulated Brillouin scattering," Opt. Lett. **41**, 926–929 (2016).
[194]I. Remer and A. Bilenca, "High-speed stimulated Brillouin scattering spectroscopy at 780 nm," APL Photonics **1**, 061301 (2016).
[195]G. Zanini and G. Scarcelli, "Localization-assisted stimulated Brillouin scattering spectroscopy," APL Photonics **7**, 056101 (2022).
[196]C. W. Ballmann, Z. Meng, A. J. Traverso, M. O. Scully, and V. V. Yakovlev, "Impulsive Brillouin microscopy," Optica **4**, 124–128 (2017).
[197]B. Krug, N. Koukourakis, and J. W. Czarske, "Impulsive stimulated Brillouin microscopy for non-contact, fast mechanical investigations of hydrogels," Opt. Express **27**, 26910–26923 (2019).
[198]B. Krug, N. Koukourakis, J. Guck, and J. Czarske, "Nonlinear microscopy using impulsive stimulated Brillouin scattering for high-speed elastography," Opt. Express **30**, 4748–4758 (2022).
[199]I. Remer, R. Shaashoua, N. Shemesh, A. Ben-Zvi, and A. Bilenca, "High-sensitivity and high-specificity biomechanical imaging by stimulated Brillouin scattering microscopy," Nat. Methods **17**, 913–916 (2020).
[200]F. Yang, C. Bevilacqua, S. Hambura, A. Neves, A. Gopalan, K. Watanabe, M. Govendir, M. Bernabeu, J. Ellenberg, A. Diz-Muñoz, S. Köhler, G. Rapti, M. Jechlinger, and R. Prevedel, "Pulsed stimulated Brillouin microscopy enables high-sensitivity mechanical imaging of live and fragile biological specimens," Nat. Methods **20**, 1971–1979 (2023).
[201]D. M. Chow and S.-H. Yun, "Pulsed stimulated Brillouin microscopy," Opt. Express **31**, 19818–19827 (2023).
[202]R. Shaashoua, L. Kasuker, M. Kishner, T. Levy, B. Rotblat, A. Ben-Zvi, and A. Bilenca, "Brillouin gain microscopy," Nat. Photonics **18**, 836–841 (2024).
[203]J. R. Rosvold, G. Zanini, C. Handler, E. Frank, J. Li, M. I. Vitolo, S. S. Martin, and G. Scarcelli, "Stimulated Brillouin scattering flow cytometry," Biomed. Opt. Express **15**, 6024–6035 (2024).
[204]R. Shaashoua, T. Levy, B. Rotblat, and A. Bilenca, "Enhancing mechanical stimulated Brillouin scattering imaging with physics-driven model selection," Laser Photonics Rev. **18**, 2301054 (2024).